

See discussions, stats, and author profiles for this publication at: <https://www.researchgate.net/publication/51098350>

Observation of Negative Charge Trapping and Investigation of Its Physicochemical Origin in Newly Synthesized Poly(tetraphenyl)silole Siloxane Thin Films

ARTICLE *in* JOURNAL OF THE AMERICAN CHEMICAL SOCIETY · MAY 2011

Impact Factor: 12.11 · DOI: 10.1021/ja1108112 · Source: PubMed

CITATIONS

13

READS

36

5 AUTHORS, INCLUDING:



Ki-Jeong Kim

Seoul National University Bundang Hospital

81 PUBLICATIONS 553 CITATIONS

[SEE PROFILE](#)



Honglae Sohn

Chosun University

135 PUBLICATIONS 1,647 CITATIONS

[SEE PROFILE](#)



Hyun-Dam Jeong

Chonnam National University

47 PUBLICATIONS 375 CITATIONS

[SEE PROFILE](#)

Observation of Negative Charge Trapping and Investigation of Its Physicochemical Origin in Newly Synthesized Poly(tetraphenyl)silole Siloxane Thin Films

Jin-Kyu Choi,[†] Seunghyun Jang,[‡] Ki-Jeong Kim,[§] Honglae Sohn,^{*,†} and Hyun-Dam Jeong^{*,†}

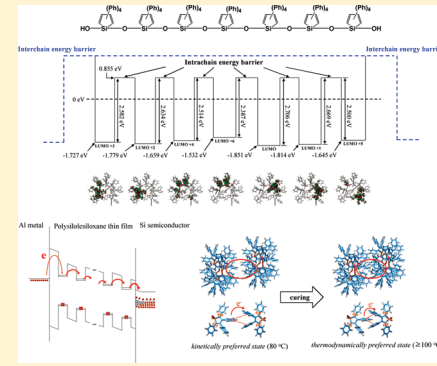
[†]Department of Chemistry, Chonnam National University, Gwangju 500-757, Republic of Korea

[‡]Department of Chemistry, Chosun University, Gwangju 501-759, Republic of Korea

[§]Pohang Accelerator Laboratory, Pohang University of Science and Technology, Pohang 790-784, Republic of Korea

Supporting Information

ABSTRACT: A new kind of organic–inorganic hybrid polymer, poly(tetraphenyl)silole siloxane, was invented and synthesized for realization of its unique charge trap properties. The organic portions consisting of (tetraphenyl)silole rings were responsible for negative charge trapping, while the Si–O–Si inorganic linkages provided the intrachain energy barrier for controlling electron transport. The polysilole siloxane dielectric thin films were fabricated by spin-coating and curing of the polymers, followed by characterization with spectroscopic ellipsometry (SE), near edge X-ray absorption fine structure spectroscopy (NEXAFS), and photoemission spectroscopy (PES). The abrupt increase in density and decrease in thickness of the thin film at a curing temperature of 100 °C was attributed to a *thermodynamically preferred state* in the nanoscopic arrangement of the polymer chains; this was due to cofacial π–π interactions in a skewed manner between peripheral phenyl groups of the (tetraphenyl)silole rings of the adjacent polymer chains. Using the NEXAFS spectrum to assess high electron affinity, the LUMO energy level of the dielectric thin film cured at 150 °C was positioned 1 eV above the Fermi energy level (E_F). The electron trapping of the dielectric thin films was confirmed from the positive flat band shift (ΔV_{FB}) in the capacitance–voltage (C – V) measurements performed within the metal–insulator–semiconductor (MIS) device structure, which strongly verified the polymer design concept. From the simple kinetics model of the electron transport, it was proposed that the flat band shift (ΔV_{FB}) or trap density of the negative charges ($|\rho|$) was logarithmically proportional to the decay constant (β) for the electron-tunneling process. When a phenyl group of a silole ring in a polymer chain was inserted into the two available phenyl groups of another silole ring in another polymer chain, the electron transfer between the groups was enhanced, decreasing the trap density of the negative charges ($|\rho|$). For the *thermodynamically preferred state* generating the high refractive index, the distance between the two phenyl groups of the adjacent polymer chains was estimated to be in the range of 0.27–0.36 nm.



INTRODUCTION

Compared to the materials made entirely from either organic or inorganic components only, organo–inorganic hybrid materials are materials in which organic and inorganic components are mixed at a molecular level to give superior mechanical, thermal, optical, and electrical properties.^{1–3} The nanostructures and physical properties of the organic–inorganic hybrid materials are dependent upon not only the molecular structure of the organic or inorganic components themselves but also their synergistic effects. One of the most crucial points in designing new organic–inorganic hybrid materials is to consider the type of chemical bonds and interfacial area between the organic and inorganic components from which its physical properties will be controlled. These materials are basically classified into two types according to the nature of the interface. In class I type materials, no covalent or ionic bonds are present between the organic and inorganic components, whereby the material is simply synthesized by embedding organic components within growing

inorganic networks. This is generally processed by chemical interactions through H-bonding and π-bonding.^{4,5} In class II type materials, part of the organic and inorganic components are linked through strong chemical bonds (covalent, ionic, dative).

Polyorganosiloxane polymers are one of the most representative organic–inorganic hybrid materials of class II type in which organic groups and inorganic –Si–O–Si– moieties are connected by Si–C covalent bonds, as shown in Figure 1a. These polymers are easily synthesized from monomers containing Si–C bonds as they retain the covalent character of the sp^3 hybridization and maintain the Si–C bonds, even from nucleophilic attack.³ For example, hydrolysis/condensation polymerization (denoted sol–gel polymerization in a materials science context) with organo-substituted silicic acid esters ($R'_nSi(OR)_{4-n}$),

Received: December 2, 2010

Published: May 04, 2011

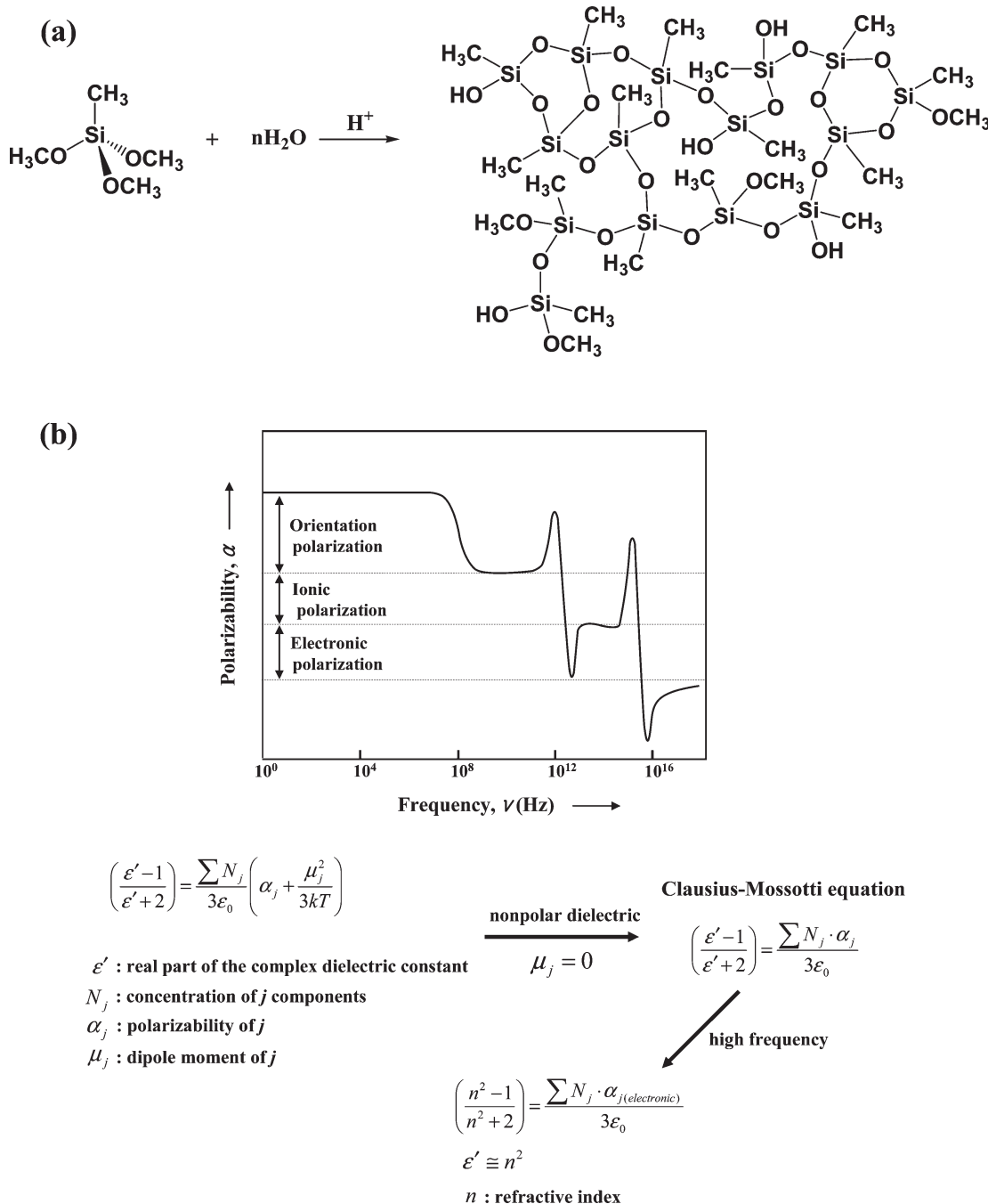


Figure 1. (a) Typical example of organic–inorganic hybrid materials: silsesquioxane polymer. The polymer is classified as a polyorganosiloxane. The Si–CH₃ groups generate a molecule-free volume to decrease the dielectric constant, while the –SiO_{3/2}— structures provide high thermal and mechanical stabilities. (b) Polarizability of a material is varied as a function of frequency. At lower frequencies, orientation, ionic, and electronic polarization mechanisms have to be counted using a Debye equation. Around the higher frequency of 4.74×10^{14} Hz (633 nm), electronic polarization is the main contributor, which is estimated by the Lorenz–Lorentz equation.

or hydrosilylation with vinyl-containing silicone and H-terminated silicone monomers, are usually employed in the syntheses of such polyorganosiloxane polymers.

The polyorganosiloxane polymers are basically dielectric materials (abbreviated as dielectrics). What kinds of materials are typically assigned to dielectrics? If electric polarization is provoked inside a material as an electric field is applied through it, the material is regarded as dielectric. Most insulator materials can be dielectrics because they demonstrate an electric polarization

phenomenon when applying an electric field. Specifically, most of the materials containing Si–O bonds, such as polyorganosiloxane polymers, are not only insulators owing to high band gap values but also dielectrics because of polarization.

In order to investigate its physical properties and dielectric applicability, it is necessary to understand *dielectric polarization*, which has been treated as relatively less important in the field of chemistry within recent decades, although being an ever comprehensive theme within physics, chemistry, materials science, and

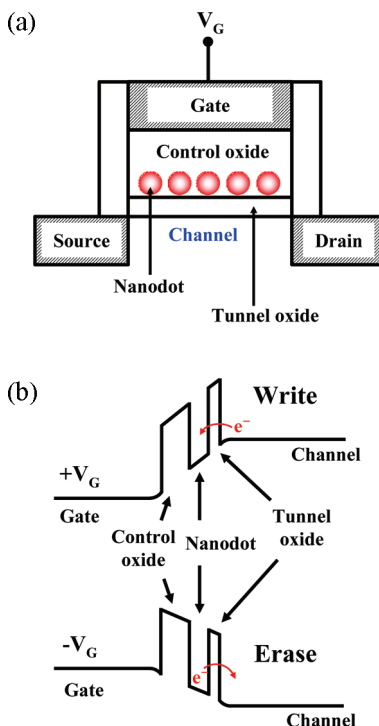


Figure 2. (a) Schematic of nanodot memory device, where nanodots are used as charge trap sites. The improved storage stability is due mainly to electrical isolation between the nanodots. (b) Writing and erasing operations of the nanodot device. An injection of an electron occurs from the channel region via direct tunneling when the control gate is forward biased with respect to the source and drain.

electrical engineering. The reason is that *the theory of dielectric polarization* was established prior to 1960; after which, application of dielectrics drew much of the attention. However, since the recent trends in the development of electronic and optoelectronic devices became necessary for highly integrated, low-cost, solution processability and large area processing, the design of new dielectrics based on *the theory of dielectric polarization* has become more strongly recommended.^{6,7} The design and synthesis of low dielectric constant materials (low-*k*) using polyorganosiloxane polymers is one of the most representative examples of utilization of this theory. The presence of organic groups in polyorganosiloxanes generates molecular-free volumes that provide the decrease in its refractive index and dielectric constant, which is explained using Lorenz–Lorentz and Clausius–Mosotti equations, respectively,⁸ as summarized in Figure 1b. Moreover, the high dielectric constant in select silicate–silsesquioxane hybrid materials has been ascribed to the existence of Si–OH groups, which has been explained using Debye's equation.⁸ Interestingly, the high refractive indices of methylene–biphenylene-bridged silsesquioxane materials were also explained by considering the high electronic polarizability of the bridged methylene–biphenylene group.⁹

In addition to the dielectric polarization of the polyorganosiloxanes, in recent years, charge trap properties have also been studied as another important aspect of dielectrics within this group.^{10,11} This is the main theme of this article. The authors contend the investigation presented herein to be very important because of the potential applicability of these charge trap properties toward next-generation memory devices and flexible electronics.^{12–15}

It has been well-known that nanodot layers bearing isolated charge trap sites can be used for nanodot memory, which not

only inherits the advantages of conventional nonvolatile flash memory but also further improves the stability of information storage within the memory devices.¹⁶ The improved storage stability is due mainly to electrical isolation between the nanodots, where the memory function remains undisturbed by the charge leakage casually generated between a single nanodot and the underlying silicon layer, thereby allowing higher density and lower power operation for the memory device. One of the widespread concepts for realizing this is the manner in which silicon or gold nanoparticles are embedded in a floating gate layer fabricated with SiO₂ dielectrics; this is one of the most recent topics in electrical engineering fields, as shown in Figure 2. Injection of an electron occurs from the channel region via direct tunneling when the control gate is forward biased with respect to the source and drain. The resulting stored charges within the nanoparticles screen out the electric field coming from the control gate and modify the threshold voltage (ΔV_{th}) of the device, whose approximate magnitude for a single electron per nanoparticle is given by:^{16b}

$$\Delta V_{th} = \frac{qn_{well}}{\epsilon_{OX}} \left(t_{ctrl} + \frac{1}{2} \frac{\epsilon_{OX}}{\epsilon_{Si}} t_{well} \right) \quad (1)$$

where ΔV_{th} is the threshold voltage shift, t_{ctrl} the thickness of the control oxide under the gate, t_{well} the linear dimensional of the nanoparticle well, ϵ 's are the relative permittivities, q is the magnitude of electronic charge, and n_{well} is the density of the nanoparticles.

Moreover, the concept of hybridization of nonvolatile flash memory or nanodot memory with an organic thin film transistor (OTFT) has been also pursued.^{12–15} This is targeted at extending the advantages of the OTFT, which include low cost, solution processability, and a large area fabrication, all of which enable fabrication of memory devices onto flexible plastic substrates. Compared to conventional flash memory that employs solid-state transistors, numerous applications of flexible electronics require nonvolatile data storage. For example, in Baeg's approach, polymer electrets with demonstrated charge trapping capabilities are used as charging layers within the OTFT device, imitating floating gate layer trapping charges in the flash memory.¹² Moreover, integration of the solution-processed nanodot layer into the OTFT has been investigated, mimicking nanodot memory for the solid-state devices, where gold nanoparticles as charge trapping centers are involved with a self-assembled block copolymer.¹⁴

The authors have initiated compelling research into charge trapping polyorganosiloxane dielectrics, which can be utilized as a solution-processed floating gate layer or nanodot layer in OTFT-based nonvolatile memory devices.^{10,11} As a first trial, the authors tested a nanocomposite dielectric as the nanodot layer, wherein porphyrin molecules and ethylene-bridged silsesquioxane dielectrics were used as the charge trap center and insulating matrix in a single nanocomposite layer, respectively.¹⁰ First from this study, the charge trap properties from the capacitance–voltage measurements ($C–V$) in the metal–insulator–semiconductor (MIS) device were confirmed. In spite of this, the phase separation problem between the porphyrin molecules and the silsesquioxane dielectrics, as well as poor reproducibility in the charge trapping phenomenon, remained inevitable using this approach because of the different chemical natures of the two components. Second, the charge trap properties of the aminopropyl-silsesquioxane thin films, where

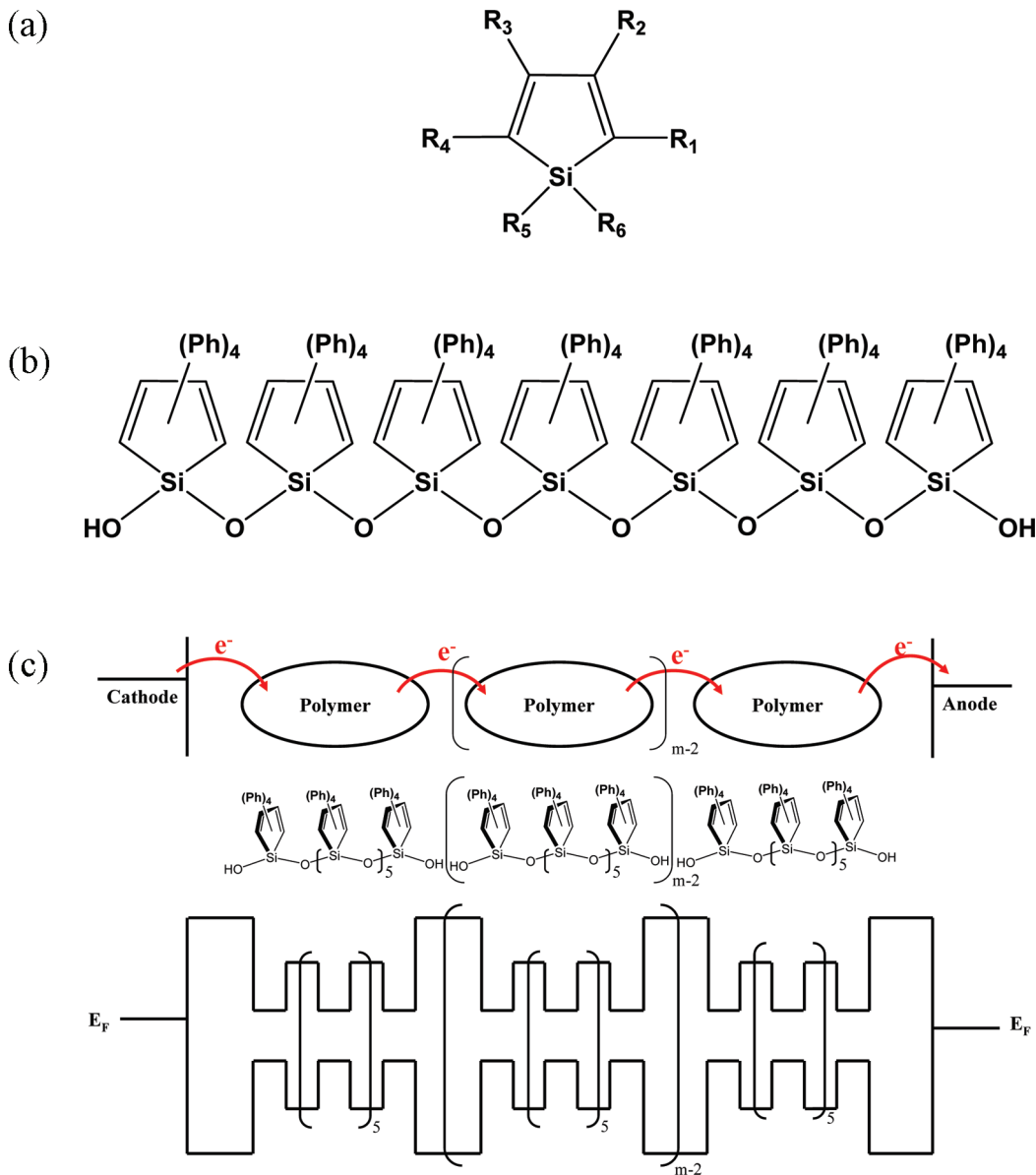


Figure 3. (a) Molecular structure of silole. R_1 , R_2 , R_3 , R_4 , R_5 , and R_6 are alkyls, aryls, or halides. (b) Molecular structure of the poly(tetraphenyl)silole siloxane polymer ($n = 7$). (c) Step potential model (SPM) for explaining electron transport through the poly(tetraphenyl)silole siloxane dielectrics. For simplification, only three polymers, wherein the number of monomers was seven ($n = 7$) for each polymer, were considered. Tentatively, the energy barrier of the interchain electron transfer was assumed to be higher than that for an intrachain transfer.

formation of two-fold $N(Si \equiv)_2$ was proposed to be the origin of electron trapping, were investigated.¹¹ The limitation of this material lies in its difficulty in engineering the charge trap density; this is due to the defect sites responsible for the electron trapping being tenuously controlled in an artificial manner.

For this article, in order to circumvent the phase separation problem and the overall lack in engineering capabilities of charge trap properties in the above two polyorganosiloxane materials, this lab adopted a new material architecture that combines the insulating properties of polyorganosiloxanes and the charge trap properties of π -conjugated organic moieties, where the two components were linked through direct covalent bonds as class II organic–inorganic hybrids. This is thought to drastically prevent the phase separation problem and allow for ease of engineering of the charge trap properties. While $-Si-O-Si-$ linkages are

maintained in the polyorganosiloxane, the directly linked organic moieties for the charge trap properties can be chosen in a variety ways from the π -conjugated molecules. This is due to the low HOMO–LUMO gap of their π -conjugated organics that usually allows for high electron affinities and low ionization energies, thus enhancing charge trapping in real applications of the devices. Among the various organic moieties this lab has been keenly interested in is the silacyclopentadiene (silole) ring for use as a charge-trapping center, whose molecular structure is shown in Figure 3a. In the silole, the LUMO energy level was much lower compared to other heteroaromatic molecules, due to mixing of the σ^* orbital of the silicon atom with the π^* orbital of the butadiene moiety.¹⁷ It is anticipated that this low-lying LUMO facilitates electron capture from the Fermi energy level of the adjacent metal or semiconductor layers. Then, in the case of using materials

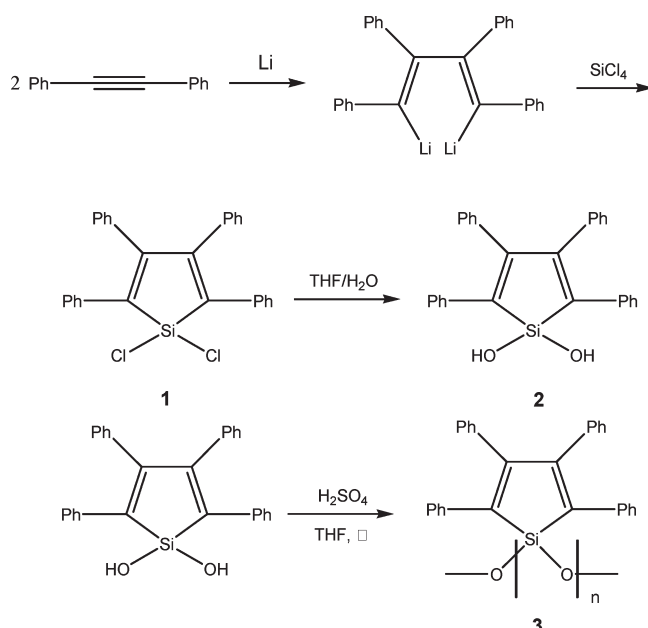


Figure 4. Schematic of poly(tetraphenyl)silole siloxane synthesis.

containing the silole moiety within the charge trap memory, substantial enhancement of electron trapping is expected.

In addition to the schematic of the hybridized polymer, poly(tetraphenyl)silole siloxane (Figure 3b), the schematic of the tentative one-dimensional potential energy diagram is displayed in Figure 3c, where electrons inside the film are trapped or transported through the polymer. The design concept is introduced in this article for the first time, through comprehensive discussion within a creative atmosphere between Prof. Jeong and Prof. Sohn, the authors of this article, who seriously considered the above arguments for the polyorganosiloxanes and charge trap properties. Shown in Figure 4 is the synthetic scheme of the poly(tetraphenyl)silole siloxane polymer, which proceeds via synthesis of dichloro(tetraphenyl)sirole (1) and dihydroxy(tetraphenyl)sirole (2).

The importance and impact of this work, from the viewpoint of chemistry or materials science, are that advancing considerations of the physical properties or functions required for materials applications leads to a contrived design of the unique molecular structure and subsequent first synthesis of the material.

As shown in the schematic of Figure 3c, the quantum well structures with energy barriers of step potential are included artificially in the hybrid materials for inducing charge trap properties. Energy barriers originated from the $-\text{Si}-\text{O}-\text{Si}-$ linkages of the high band gap, while the midgap-state trapping charges are created from the HOMO and LUMO energy levels of the π -conjugated (tetraphenyl)silole rings. Naturally, at this moment, it is difficult to present a method for theoretical estimation of the energy barrier and width of the quantum wells for a polysilole siloxane polymer, although they are pursued through DFT calculations within this article. Instead, only through successful synthesis of the materials will it be possible to experimentally validate the charge trap behavior; capacitance–voltage ($C-V$) measurements, a very well-known experimental method in electrical engineering and memory device fields, were taken of the metal–insulator–semiconductor (MIS) device.^{11,18}

In this article, for the first time, this lab synthesized a poly(tetraphenyl)silole siloxane polymer; its thin films were artificially

designed to realize charge trap properties with solution processability. This was followed by investigation of the charge trap properties using the MIS device of the polymer, which was discussed in terms of its electronic structure.

EXPERIMENTAL SECTION

2.1. Theoretical Methods. The geometries of the molecules were preoptimized using the PM3 semiempirical method in the Hyperchem 8.0 package. The ground-state geometries were then fully optimized using the density functional theory (DFT) at the B3LYP level and 6-31G** basis set in Gaussian03.

2.2. Materials. All synthetic manipulations were carried out under an atmosphere of dry argon gas using standard vacuum-line Schlenk techniques. All solvents, such as diethyl ether, THF, hexane, and toluene were purchased from Aldrich Chemical Co. Inc. (St Louis, MO, USA) and distilled from sodium/benzophenone ketyl. All other reagents, such as diphenylacetylene, lithium wire, silicon tetrachloride, and sulfuric acid were purchased from Aldrich Chemical Co. Inc. and used without further purification.

2.3. Synthetic Procedures. *Synthesis of Dihydroxy(tetraphenyl)sirole (2).* Synthesis of dihydroxy(tetraphenyl)sirole (2) is summarized schematically in Figure 4. The synthesis of dichloro(tetraphenyl)sirole (1) is previously reported.¹⁹ To synthesize the dihydroxy(tetraphenyl)sirole (2), dichloro(tetraphenyl)sirole (1) (2.0 g, 4.5 mmol) was dissolved into 50 mL of aqueous THF ($\text{THF}/\text{H}_2\text{O} = 4/1$) and stirred at room temperature for 2 h under an Ar atmosphere. The resulting mixture was then extracted with ether. The extract was washed with distilled water and brine, dried over anhydrous Mg_2SO_4 , and filtered. The filtrate was condensed under reduced pressure to give pure (2) (1.76 g, 4.2 mmol) in 94% yield as a bright-green solid: ^1H NMR (CDCl_3) $\delta = 6.8-7.2$ (m, 20H), 3.0 (s, 2H) (Supporting Information, Figure S2)

Synthesis of Poly(tetraphenyl)sirole Siloxane (3). Synthesis of poly(tetraphenyl)sirole siloxane (3) is summarized schematically in Figure 4. Dihydroxy(tetraphenyl)sirole (2) (1.0 g, 2.3 mmol), dissolved in 50 mL of THF, was refluxed with 3.0 mL of sulfuric acid as a catalyst for polymerization over 2 d. After polymerization, the solvent was dried under reduced pressure. The residual solid was dissolved in 5.0 mL of THF and poured into 100 mL of hexane. Polysilole siloxane (3) (0.6 g, 60% yield) was obtained as a light-brown powder after the third cycle of dissolution–precipitation.

2.4. Analysis of Poly(tetraphenyl)sirole Siloxane (3). *Gel Permeation Chromatography.* Molecular weights were measured by gel permeation chromatography (GPC) using a Perkin-Elmer series 200 equipped with Varian Polymer Laboratories columns (PLgel 5 μm Mixed-C and Mixed-D) with freshly distilled THF as the eluent. Molecular weights were calibrated by polystyrene standards (Varian, Easical PS-1).

Nuclear Magnetic Spectroscopy. NMR-grade deuteriochloroform was stored over 4 Å molecular sieves. All NMR data were collected with Bruker 300 MHz spectrometers (300.1 MHz for ^1H NMR and 75.5 MHz for ^{13}C NMR). Chemical shifts are reported in parts per million (ppm); downfield shifts are reported as positive values from tetramethylsilane (TMS) standard at 0.00 ppm. Samples were dissolved in CDCl_3 unless otherwise stated. ^{13}C NMR was recorded as proton-decoupled spectra.

Fourier Transform Infrared Spectroscopy. In order to investigate the molecular structure of the dihydroxy silole and the polysilole siloxane, Fourier transform infrared spectroscopy (FT-IR) was implemented. The measurements were conducted on a Nicolet 380 spectrometer operated in the mid-IR range of $4000-400 \text{ cm}^{-1}$, with all spectra obtained at a spectral resolution of 7.7 cm^{-1} in the transmittance mode.

Thermogravimetric Analysis (TGA). TGA was performed on a METTLER TOLEDO SDTA851e. The polysilole siloxane powder was placed in an aluminum oxide (AlOx) TGA pan. The sample was

heated at a rate of $10\text{ }^{\circ}\text{C min}^{-1}$ from 30 to $800\text{ }^{\circ}\text{C}$ under a nitrogen gas flow of 50 mL min^{-1} .

2.5. Synthesis and Characterization of Poly(tetraphenyl)silole Siloxane Thin Films. *Spin-Coating Process.* A 4 wt % poly(tetraphenyl)silole siloxane (**3**) solution in tetrahydrofuran (THF) was obtained by mixing 0.078 g of poly(tetraphenyl)silole siloxane (**3**) powder with 1.87 g of THF in an air atmosphere for 5 min in a vial that was previously cleaned with ethanol and acetone. Then, the 4 wt % solution was filtered (PTFE, 0.2 μm), followed by spin-coating onto a p-type silicon wafer at 2000 rpm for 25 s, respectively. The used Si-wafer had been cleaned with ethanol and acetone prior to use as a substrate. Then, the spin-coated thin films were heated at $80\text{ }^{\circ}\text{C}$ on a hot plate for 10 min in an air atmosphere to remove all remaining solvent. Finally, the thin films were cured in a vacuum tube furnace under a pressure of approximately 1.0×10^{-2} Torr for 1 h at each temperature of 100, 150, 200, and $350\text{ }^{\circ}\text{C}$. The final poly(tetraphenyl)silole siloxane thin films will be abbreviated as polysilole siloxane thin films in the remaining sections of this article.

X-ray Photoelectron Spectroscopy. Compositional changes according to different curing temperatures were recorded by X-ray photoelectron spectroscopy (XPS) measurements conducted on a MultiLab 2000 using a Mg K α (1253.6 eV) source at a pass energy of 20 eV and under a pressure of 1.0×10^{-9} Torr. An Ar $^{+}$ ion gun sputtering of 2 min at a power of 2 kV and 1.3 μA was used for a brief cleaning of the surface of the samples prior to measurement.

Fourier Infrared Spectroscopy. The changes in molecular structures of the polysilole siloxane thin films with increasing curing temperature were investigated by FT-IR. The measurements were conducted on a Nicolet 380 spectrometer operated in the mid-IR range of $4000\text{--}400\text{ cm}^{-1}$, with all spectra obtained at a spectral resolution of 7.7 cm^{-1} in the transmittance mode.

Spectroscopic Ellipsometry Measurements. The thicknesses and refractive indices of the polysilole siloxane thin films with each curing temperature were measured by spectroscopic ellipsometry (SE) with an M2000D (J.A. Wollam Co. Inc., Lincoln, NE, USA).

2.6. Surface Science Spectroscopy. Near-Edge X-ray Fine Structure Spectroscopy. The near-edge X-ray fine structure spectroscopy (NEXAFS) spectra at the C K-edge were measured at the 2B1 PES beamline of Pohang Accelerator Laboratory (PAL) in the partial electron yield (PEY) detection mode with a retarding voltage of -210 V and an accelerating voltage of 1.6 kV . Molecular bonding information for the surface of the polysilole siloxane thin films cured at $150\text{ }^{\circ}\text{C}$, from poly(tetraphenyl)silole siloxane (**3**) solutions of 0.1, 0.4, 1, and 4%, was obtained from the PEY mode NEXAFS spectra by considering probing depths less than 10 \AA . The data were first normalized by the current of the clean Au mesh to remove the monochromator structure due to adsorbed carbon on the optical elements of the beamline. Second, the edge jump was set to 1 for all spectra to remove contributions from the emission angle, beam decay, and effective spot size on the sample. The photons showed a polarization of 85% with an incident photon energy resolution of 350 meV near the carbon K-edge region.

High-Resolution Core-Level and Valence Band Photoemission Spectroscopy. High-resolution photoemission spectroscopy (HRPES) was introduced to investigate the chemical structure of the polysilole siloxane thin films. All HRPES experiments were performed at the 8A2 beamline at the Pohang Accelerator Laboratory (PAL), which is equipped with an electron analyzer (SES100, Gamma Data Scientia). Depending on the wt % of the poly(tetraphenyl)silole siloxane solutions, the O 1s, C 1s, Si 2p, and valence band spectra were measured accordingly. The total spectral resolution was less than 200 meV at a photon energy of 635 eV for Si 2p, O 1s, and C 1s, with a photon energy of 130 eV for Si 2p and a valence band at 8A2 HR-PES beamline in the Pohang Accelerator Laboratory (PAL). The binding energy of the C 1s and O 1s were calibrated by measuring the Si 2p core level of the silicon substrate. All spectra were recorded in the normal emission mode.

2.7. Fabrications and Measurements of Device Structures for Electrical Properties. MIS Structures. Metal–insulator–semiconductor (MIS) device structures were fabricated to investigate the capacitance–voltage ($C\text{--}V$) characteristics. Aluminum metal, as a top electrode, was thermally deposited onto the polysilole siloxane thin films where low-doped Si(100) wafers (resistivity: $1\text{--}30\text{ }\Omega\cdot\text{cm}$, thickness: 525 nm) were used as a semiconductor layer. The backside of the Si wafer in the MIS devices was also coated with Al metal to diminish contact resistance.

Capacitance–Voltage Measurements. An HP4284 LCR meter was used to obtain the $C\text{--}V$ curves by applying an ac voltage with a frequency of 1 MHz and an amplitude of 1 V to the top aluminum electrode, with a dc bias voltage swept over a range of -35 to 35 V on the MIS devices. The $C\text{--}V$ curves were recorded in both forward and reverse directions, and afterward, in order to investigate the charge trap mechanisms.

■ RESULTS AND DISCUSSION

This article comprises various data and interpretations in diverse areas: DFT calculations in Gaussian03,²⁰ polymer syntheses; thin film characterizations; photoemission and photoabsorption spectroscopy; device physics. This comprehensive, yet somewhat complex composition, proved unavoidable in order to accomplish the research goal: invention of poly(tetraphenyl)silole siloxane and realization of negative charge trapping. Its certain consequence is complexity in interpretation of the data and randomness in proving the point of this article.

In order to maintain clearness within a proper scientific context throughout this section, the authors have adopted the viewpoint of electron theory, whereby the probability amplitude and energy of electrons are treated as the main factors in determining the physical properties of a material, especially electrical and optical properties, which have recently become very common in chemistry, materials science, and electrical engineering fields.²¹ This framework is based upon quantum mechanics and solid-state physics. A different aspect of this article, compared to conventional electron theory, is that the nature of the electrons in the poly(tetraphenyl)silole siloxane thin films (abbreviated polysilole siloxane thin films throughout the rest of the article) is described only in a qualitative manner, given the theoretical limitations of the organic–inorganic hybrids. Another important feature of this article is that energy and location of the electrons are estimated from the molecular orbitals of the poly(tetraphenyl)silole siloxanes instead of using the band theory. This is because the polysilole siloxane thin films can be regarded as molecular solids, of which the building blocks are molecules or polymers. Within the authors' knowledge base, there exists no conclusive or established theory that accounts for the electron dynamics within molecular solids. Because of this theoretical limitation, the authors first calculated the energy level of the molecular orbitals of the poly(tetraphenyl)silole siloxane and applied its main results toward explaining the charge trap properties of the polysilole siloxane thin films.

DFT Calculations of Dihydroxy(tetraphenyl)silole and Poly(tetraphenyl)silole Siloxane. The DFT calculation results are summarized in Figure 5. Figure 5a shows the calculated orbital energy levels of dihydroxysilacyclopentane, dihydroxysilacyclopentadiene (dihydroxysilole), and dihydroxy(tetraphenyl)silole (**2**), a series of poly(tetraphenyl)silole siloxanes with a number of tetraphenylsiloles represented by a select number of silicon atoms (**2**–**7**), and the polydimethylsiloxane within the energy range of 2 to $\sim -10\text{ eV}$. The highest occupied molecular orbitals (HOMOs) and lowest unoccupied molecular orbitals (LUMOs)

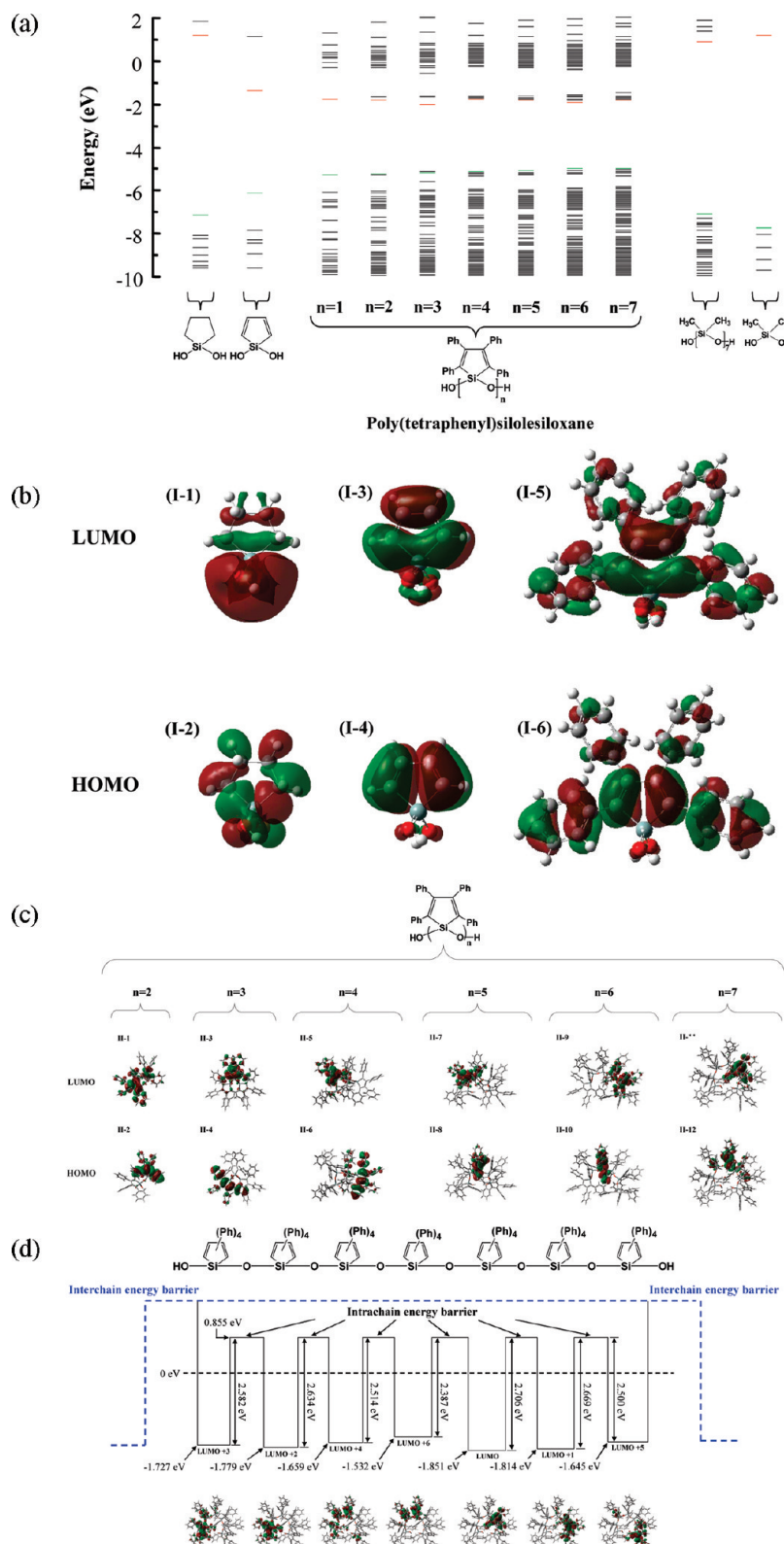


Figure 5. (a) Molecular orbital energy diagram for optimized geometries. Geometry optimization was performed using DFT calculations in the Gaussian 03 packages. For the poly(tetraphenyl)silole siloxanes, the density of states is increased as n is increased. In order to estimate the barrier height due to the $-\text{Si}=\text{O}-\text{Si}-$ linkage, the energies of the molecular orbitals of the polydimethylsiloxane were also obtained and compared. (b) Shapes of HOMOs and LUMOs of dihydroxysilole. (c) HOMO and LUMO drawings of polysilole siloxanes (from $n = 2$ to $n = 7$). (d) Step potential model of polysilole siloxane ($n = 7$). The barrier heights were estimated from the LUMO of polydimethylsiloxane ($n = 7$) and unoccupied orbitals of poly(tetraphenyl)silole siloxane ($n = 7$). The barrier heights for the interchain electron transfer were arbitrarily set, which may be higher for explaining the energy barrier of the intrachain electron transfer.

are respectively denoted by the green and red colors. By comparing dihydroxysilacyclopentane and dihydroxysilole, the HOMO energy becomes higher and the LUMO energy lower through addition of π bonds into the silacyclopentyl ring. Here, the low LUMO energy is partly due to the σ^* – π^* conjugation between the σ^* orbital of the silicon and the π^* orbital of the butadiene.¹⁷ This σ^* – π^* conjugation can be also understood with the LUMO electron density isocontour plots of the dihydroxysilacyclopentane and dihydroxysilole in I-1 and I-3 of Figure 5b. The LUMO of the dihydroxysilole is primarily delocalized through π -bonded carbons and the silicon atom, confirming the σ^* – π^* conjugation as reported.^{17,22} In addition, the HOMO energy of the dihydroxysilole was higher than that of the dihydroxysilacyclopentane, as shown in Figure 5a, because the HOMO arises mainly from the π orbitals of the butadienyl rings as shown in I-4 of Figure 5b, compared to that of the dihydroxysilacyclopentane from the σ orbitals (I-2 of Figure 5b).

When the orbital energies of the dihydroxysilole and the dihydroxy(tetraphenyl)silole (**2**, $n = 1$) are compared in Figure 5a, the HOMO energy increased considerably by addition of phenyl substituents on the silole ring, while the LUMO energy only slightly decreased. As shown in I-5 and I-6 of Figure 5b, the LUMO and HOMO orbitals are spread out mainly on the silole ring, as well as the phenyl groups.

Variation in the electronic structure of the poly(tetraphenyl)silole siloxane, according to the number of (tetraphenyl)siloles counted by the number of silicon atoms (1–7), was theoretically investigated as well. It is noteworthy that the energies of the HOMO and LUMO were little affected upon increasing the number of tetraphenylsiloles, although many occupied and unoccupied orbitals were newly generated. As shown in Figure 5c, the HOMOs and LUMOs for the poly(tetraphenyl)silole siloxanes were similar to those of the dihydroxy(tetraphenyl)siloles, indicating that the HOMOs and LUMOs of the (tetraphenyl)siloles in the polymer do not significantly interact with each other due to the high energy barrier originating from the Si–O–Si linkages.

The intrachain energy barrier generated by the σ and σ^* orbitals of the Si–O–Si linkages in the poly(tetraphenyl)silole siloxane was indirectly estimated from corresponding orbital energies of the polydimethylsiloxanes, which have the same skeleton structure as the poly(tetraphenyl)silole siloxane, as there are so many energy levels for the polysilole siloxane polymer that the σ and σ^* orbitals were not distinctly found. As indicated in Figure 5a, the HOMO and LUMO energies for the dimethylsiloxane were calculated to be –7.815 and 1.167 eV, respectively. In addition, the HOMO and LUMO energies for the polydimethylsiloxane ($n = 7$) were calculated to be –7.160 and 0.855 eV, respectively, which are regarded as the energies of the highest σ and lowest σ^* orbitals for poly(tetraphenyl)silole siloxane ($n = 7$), as mentioned above. Then, the energy barrier for an electron occupying the LUMO in poly(tetraphenyl)silole siloxane ($n = 7$) was estimated as follows:

energy barrier (eV)

$$\begin{aligned} &= \text{the energy of lowest } \sigma^* \text{ orbitals in polydimethylsiloxane } (n = 7) \\ &- \text{the energy of } \pi^* \text{ orbitals in poly(tetraphenyl)silole siloxane } (n = 7) \\ &= 0.855 - (-1.851) = 2.706 \text{ (eV)} \end{aligned}$$

However, the LUMO was localized mainly on the fifth silole ring on the polymer chain, as shown in Figure 5c,d, indicating that the energy and spatial variation in the energy barriers have to be

carefully counted. This is very simply demonstrated using a step potential model (SPM), which is typically employed for describing the electronic states in conjugated hydrocarbon molecules.²³ As shown in Figure 5d, the simple step potential model for the poly(tetraphenyl)silole siloxane ($n = 7$) was built up by using the energies and orbital shapes of the seven lowest unoccupied orbitals from LUMO to LUMO + 6. Through the siloxane chain, there are seven quantum well structures, each possessing different energy values. The authors hold that these quantum well structures are the origin of the electron trapping of the poly(tetraphenyl)silole siloxane polymers in the condensed phase, which will be applied toward interpretation of the following capacitance–voltage (C–V) results in a metal–insulator–semiconductor (MIS) device of the polysilole siloxane thin films.

In addition to the intrachain energy barriers, the interchain energy barrier was also displayed as a dotted line, as shown in Figure 5d. This is not actually one-dimensional as it surrounds the seven quantum wells in three-dimensional space through the polymer chain. The width and height of the interchain energy barrier relies mainly on the two nearest located (tetraphenyl)silole rings of the two adjacent polymer chains. The electron transfer rate between the two adjacent polymer chains, one of the decisive control factors of the electron trapping, is surely believed to be more controlled by the interchain energy barriers than by the intrachain energy barriers.

An important issue to consider is whether the interchain energy barrier exists. Even if the interchain energy barrier did not exist, electron trapping would likely be observed due to the intrachain energy barrier. Nevertheless, the authors speculate that nonexistence of the interchain energy barrier in such molecular solids is forbidden because there would only be van der Waals interactions between the polymer chains instead of direct covalent bonds. Conversely, the authors would, without reservation, suggest that existence of the intrachain energy barrier strengthens the effects of the interchain energy barrier on the charge trapping phenomena in an additional way. This is because, in the case of having an intrachain energy barrier, the effective cross-section area of the electron transfer between the two adjacent polymer chains is smaller than when there is no intrachain energy barrier. It is the contention of the authors that this is the real meaning of existence of the intrachain energy barrier for charge trapping events, even in the presence of an interchain energy barrier. An effective way to address this issue is to directly calculate the interchain energy barriers of the poly(tetraphenyl)silole siloxane and poly(tetraphenyl)silole using the Marcus theory and compare with the other. Here, the poly(tetraphenyl)silole does not include –Si–O–Si– linkages; thus, it lacks any intrachain energy barriers through the polymer chain. These kinds of theoretical calculations are being planned with intent for submission in a separate paper.

Undoubtedly, energetic and spatial criteria in this quantum well structure, such as barrier heights and well widths, are highly dependent upon optimized polymer geometry. This argument is very important for interpretation of the effects of the nanoscopic arrangements of the polymers upon the electrical properties of the thin films of the poly(tetraphenyl)silole siloxane, as will be discussed below. It also allowed the theoretical basis that the physical properties of the polymer are highly sensitive to the process conditions for depositing the thin films of the polymer (formation of molecular solids).

Synthesis and Characterization of Dihydroxy(tetraphenyl)silole and Poly(tetraphenyl)silole Siloxane. The weight-averaged molecular weight (M_w) and polydispersity (M_w/M_n) of

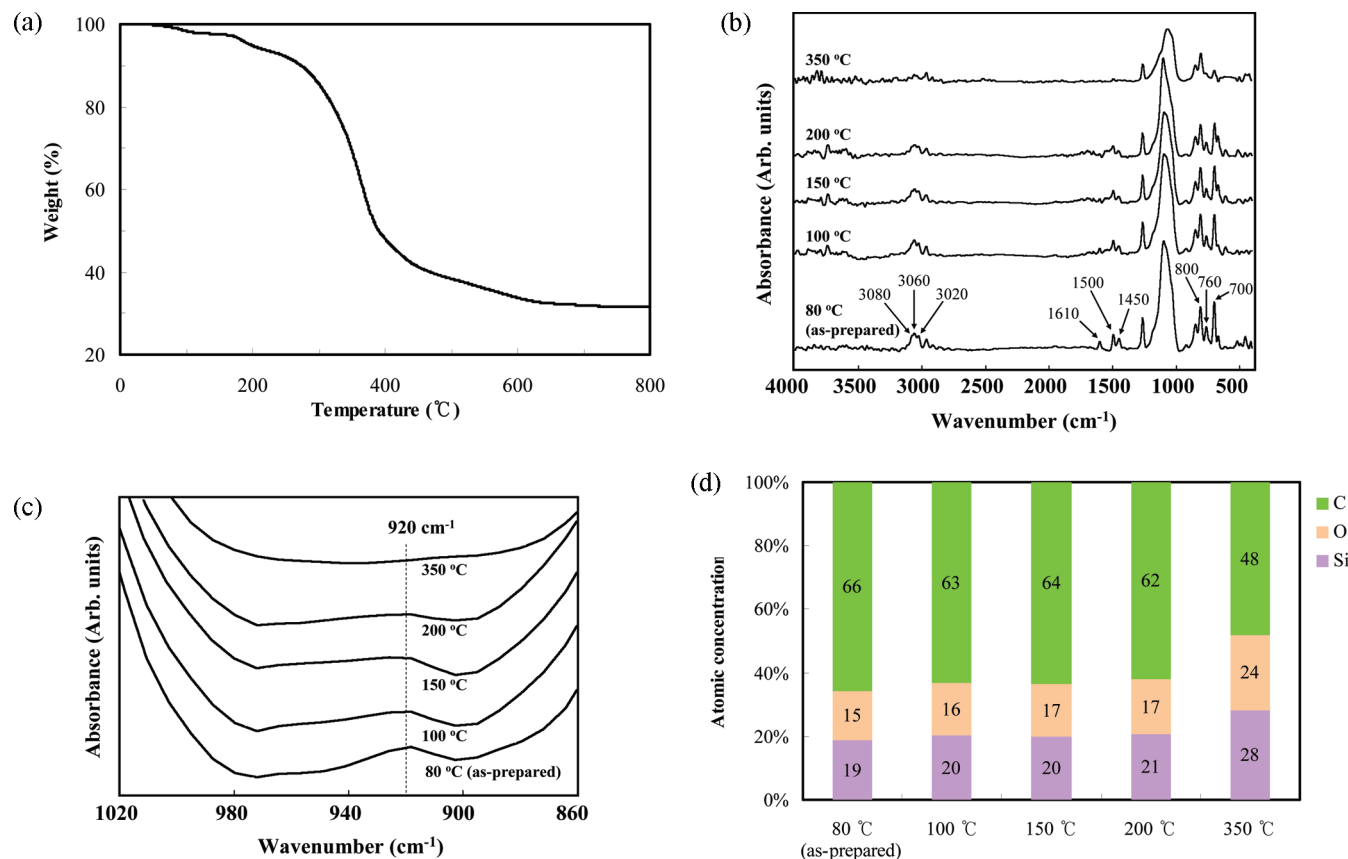


Figure 6. (a) Thermogravimetric analysis results of the poly(tetraphenyl)silole siloxane polymer. The abrupt decrease in weight was observed around 280 °C. (b) Changes in the FT-IR spectra for the poly(tetraphenyl)silole siloxane thin films according to curing temperatures. (c) Change in the peak at about 920 cm⁻¹ in the FT-IR spectra, indicating a gradual decrease in intensity of the Si—OH groups with an increase in curing temperature. (d) Changes in the chemical composition of poly(tetraphenyl)silole siloxane thin films, according to curing temperatures, investigated from XPS analysis results.

polysilole siloxane polymer **3** were measured at approximately 3087 and 1.18, respectively, using GPC (Supporting Information, Figure S1). Since the molecular weight of the dihydroxy(tetraphenyl)silole monomer (**2**) is 418.6, the poly(tetraphenyl)silole siloxane (**3**) consists of nearly seven monomers on average. As such, the lab focused upon the polymer of seven monomers in Figure 3b and c and Figure 5a,c,d, and the related results and discussion. The synthesis of **3** was confirmed by NMR (Supporting Information, Figure S2).

The TGA results of the poly(tetraphenyl)silole siloxane (**3**) polymer are shown in Figure 6a. Weight loss began at 90 °C by evaporation of physisorbed water molecules, with additional weight loss from approximately 170 °C related to the condensation reaction of the Si—OH groups. The possibility of the condensation reaction is also supported by the following FT-IR results of the polysilole siloxane thin films. Above 280 °C, a huge loss in weight was observed, due to thermal decomposition of the organic sections, as also mentioned in the below FT-IR data.

Synthesis and Characterization of Polysilole Siloxane Thin Films. Figure 6b shows the FT-IR spectra of the poly(tetraphenyl)silole siloxane thin films (abbreviated polysilole siloxane thin films) at different curing temperatures. The peaks at 3080, 3060, and 3020 cm⁻¹ are attributed to the stretching of the sp²-hybridized C—H, while the peaks at 760 and 700 cm⁻¹ were assigned to the bending of C—H in the monosubstituted aromatic groups,²⁴ implying the existence of phenyl groups in the

polysilole siloxane thin films. The peaks in the range of 1600–1400 cm⁻¹ were ascribed to the stretching of C=C in the phenyl groups,²⁴ as well as silole rings.

The inorganic sections (Si—O—Si linkages) were also confirmed by the peaks at 1200–1000 cm⁻¹, attributed to their antisymmetric stretching, and the peak at 800 cm⁻¹, assigned to their symmetric stretching.²⁵ The position of the Si—O—Si antisymmetric stretching peak was highly dependent upon the local bonding geometry of the Si—O—Si linkages. The peak position is maintained at approximately 1100 cm⁻¹ during the curing temperatures, up to 200 °C, which is evidently due to the Si—O—Si.

Moreover, the terminal Si—OH groups were detected at about 920 cm⁻¹,²⁶ the intensity of which gradually decreased with increasing curing temperature, as shown in Figure 6c. As the curing temperature increased, the peaks indicating the organic groups gradually decreased, but only slightly. Above 200 °C, decomposition of the organic species accelerated, consistent with the TGA results in Figure 6a and the XPS results in Figure 6c. Finally, the organic species disappeared to a considerable extent at curing temperatures of 350 °C. Figure 6d shows variations in the chemical composition of the polysilole siloxane thin films according to the curing temperature.

This lab measured refractive index using spectroscopic ellipsometry according to the curing temperatures shown in Figure 7a,b. The refractive indices of the thin films were abruptly increased as the curing temperature increased from 80°

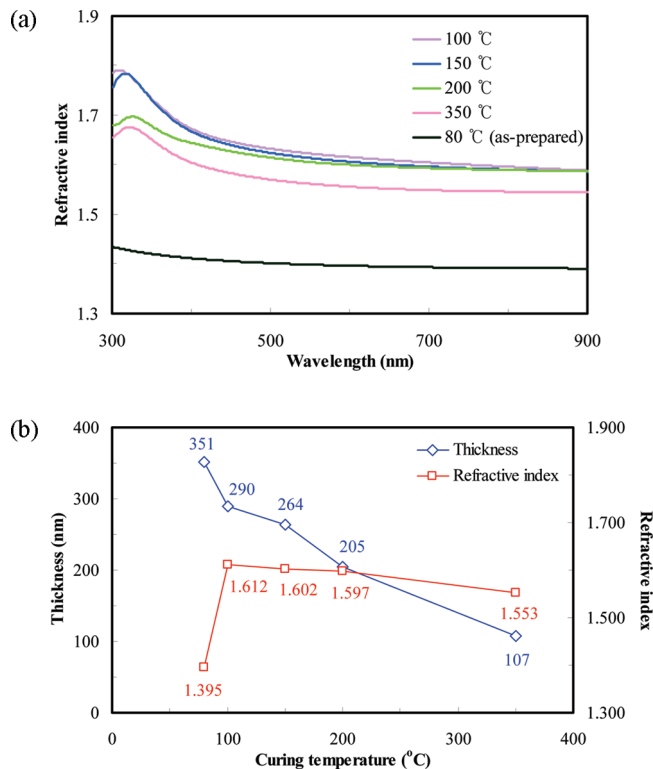


Figure 7. Spectroscopic ellipsometry results. (a) Refractive indices of poly(tetraphenyl)silole siloxane thin films. The abrupt increase in refractive index was observed as the curing temperature increased from 80 to 100 °C. At higher curing temperatures, the refractive indices gradually decreased with increasing curing temperatures. (b) Changes in refractive indices and film thicknesses according to curing temperature.

(as prepared) to 100 °C, while decreasing slightly at higher temperatures. The refractive index was closely related to the density of the thin films, which was supported by the following Lorenz–Lorentz equation,^{6,8} as briefly explained in the Introduction and Figure 1b:

$$\left(\frac{n^2 - 1}{n^2 + 2} \right) = \frac{\sum N_j \cdot \alpha_{j(\text{electronic})}}{3\epsilon_0} \quad (2)$$

where n is the refractive index, N_j density, $\alpha_{j(\text{electronic})}$ electronic polarizability, and ϵ_0 vacuum permittivity. As explained in detail in the Supporting Information (Figure S3), the refractive index (n) is directly proportional to N_j and $\alpha_{j(\text{electronic})}$, in the range of the refractive index of the polysilole siloxane thin films.

The abrupt increase in density of the thin film cured at 100 °C is explained by a chemical kinetics model for nanoscopic arrangement and interchain interaction of the constituting polysilole siloxane polymers in the film, as summarized in Figure 8a,b. As the polymer solution was spin-coated at room temperature, the coating solvent evaporated too quickly compared to the time scale required for the polymers to be arranged on the substrate, leaving a metastable state of the polymer arrangement.²⁷ This is considered to be a *kinetically preferred state* in terms of chemical kinetics, as illustrated in Figures 8a and 13f. A curing temperature of 80 °C for the as-prepared sample is thought to be only for removal of the remaining solvent molecules trapped between the polymer chains and subsequently too low to irritate the *kinetically preferred state*. Surprisingly, the small increase (20 °C) in curing

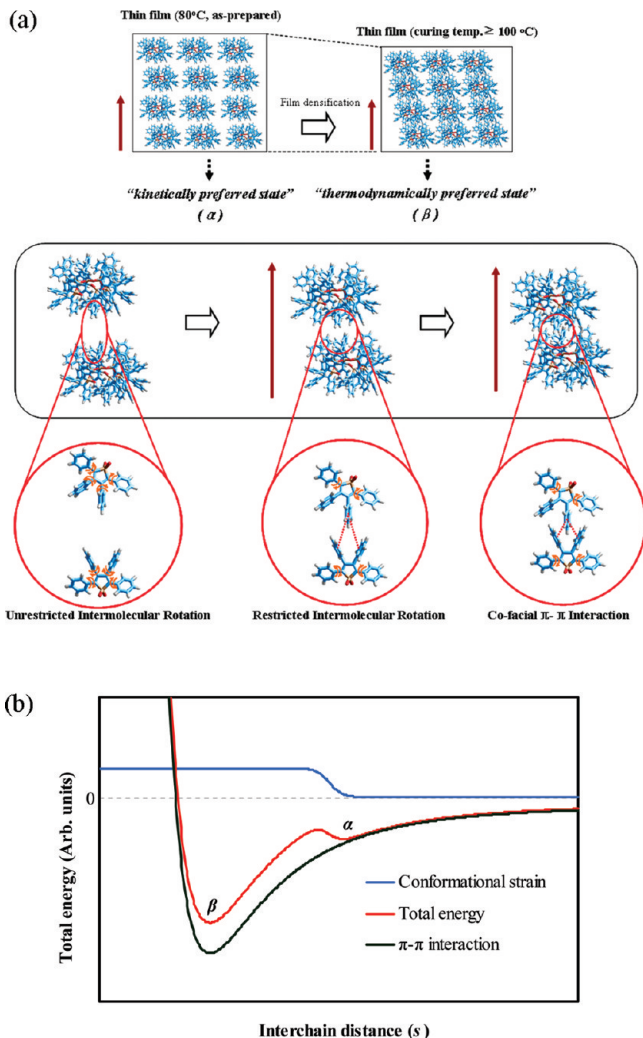


Figure 8. (a) Tentative model for nanoscopic arrangements of constituting poly(tetraphenyl)silole siloxane polymer chains inside the dielectric thin film. The geometry of the individual polymer chain was initially optimized using DFT calculations in Gaussian03 packages. Here, the number of silole rings was set to 7. At low curing temperatures (≤ 80 °C), the *kinetically preferred state* is sustained, where the silole rings stay in a dominant state of “restricted intermolecular rotation”, while, at higher curing temperatures (≥ 100 °C), the *thermodynamically preferred state* emerges where cofacial $\pi-\pi$ interactions in a skewed manner between phenyl rings bonded to the silole rings must exist. (b) Total energy graph along the interchain distance (s). The origin of the total energy of the polymer was divided into the two main components, the $\pi-\pi$ intermolecular interaction between phenyl rings of the neighboring siloles in the polymers, as mentioned above, and total conformational strains of the polymer, such as angle strains or geometry relaxation of the polymer chains.

temperature gave rise to huge differences in the refractive index values, as shown in Figure 7a,b, indicating the significant increase in density of the films. This can be understood by creating the nanoscopic model of collective interactions of the polysilole siloxanes, *thermodynamic preferred state*, as depicted in Figures 8a and 13f, which is based upon the unique molecular structure of the polysilole siloxane.

The total energy graph in Figure 8b is qualitatively drawn to explain the abrupt increase in the density of the films at a curing temperature of 100 °C. This is accomplished by introducing two models, the *kinetically preferred state* (α) for the film cured at

80 °C and the *thermodynamically preferred state* (β) for the film cured at 100 °C, both related to the nanoscopic arrangement of the polymer, all of which are summarized in Figure 8a. The authors assert that the abrupt increase in the density of the films is related to the $\pi-\pi$ intermolecular interactions between the phenyl rings of the neighboring silole groups. A theoretical evaluation of the intermolecular interaction between benzene molecules with benzene dimers of various structures, such as parallel, T-shaped, and slipped parallel cases, according to the intermolecular (benzene to benzene) distance, has been performed as model chemistry by Tanabe et al.²⁸ Though calculation of the intermolecular interaction between benzene molecules in a skewed manner, as found in our polysilole siloxane case, was not performed in their study, we proffer that their viewpoint regarding the intermolecular interaction between two benzene molecules can be applied toward our interpretation.

The total energy graph is drawn along the interchain distance (s) between the phenyl rings of the neighboring silole groups, defined in Figure 8b as the x-coordinate. The authors speculate that the origin of the total energy of the polymer is divided into two main components, the $\pi-\pi$ intermolecular interaction between the phenyl rings of the neighboring siloles in the polymers, as mentioned above, and the total conformational strains of the polymer, such as angle strains or geometry relaxation of the polymer chains. Herein, the $\pi-\pi$ intermolecular interaction energy drawn ($E_{\pi-\pi}(s)$) was previously cited²⁸ and fitted by eq A.1; the total conformational strain energy ($E_{\text{strain}}(s)$) was hypothetically drawn without direct evidence, as fitted by eq A.2:

$$E_{\pi-\pi}(s) = A \cdot \left[\left(\frac{s_0(\pi-\pi)}{s} \right)^n - \left(\frac{s_0(\pi-\pi)}{s} \right)^m \right], \quad (n > m) \quad (\text{A.1})$$

$$E_{\text{strain}}(s) = \frac{B}{1 + \exp[\beta(s - s_0(\text{strain}))]} \quad (\text{A.2})$$

where $s_0(\pi-\pi)$ and $s_0(\text{strain})$ are the specific interchain distances where the total $\pi-\pi$ interaction energy between the phenyl rings and total conformational strain energy of the polymer become minimum and half of maximum, respectively, while n and m are integers, β is a coefficient, and A and B are arbitrary constants. All of the factors are arbitrarily chosen to suitably describe the speculated physicochemical situation. This lab hypothesizes that the conformational strain energy of the polymers is nearly zero when the distance between the phenyl rings of the neighboring siloles of the polymers is far enough, then it increases when the interchain distance (s) decreases below a point. After that, the conformational strain energy is assumed to be constant. Thus, as the polymer solution was spin-coated onto the substrate at room temperature, the polymer films might remain in the α state (*kinetically preferred state*) due to the energy barrier originating from the increase in the conformational strain energy near $s_0(\text{strain})$. As the curing temperature was increased from 80 and to 100 °C, the polymer chain could overcome the energy barrier and enter into the β state (*thermodynamically preferred state*), decreasing the interchain distance (s).

The authors hold that the two local minima still exist over 100 °C, even though the β state becomes more dominant in the films as curing temperature increases. With $[\alpha]$ and $[\beta]$ as the respective concentrations of finding the α and β states in the polymer film, under thermodynamic equilibrium conditions more preferred at 100 °C than 80 °C, the ratio of the probabilities are given by the following equation, where E_α and E_β are total

energy of α and β states, respectively:

$$\frac{[\alpha]}{[\beta]} \approx \exp\left(-\frac{E_\alpha/E_\beta}{kT}\right)$$

This implies that the α state does not disappear entirely, even at 100 °C

The authors hold that the *kinetically preferred state* resembles the nanoaggregation state in terms of local polymer arrangement, which promotes aggregation-induced emissions (AIEs).²⁹ For silole-related molecules showing the AIE, restricted intermolecular interaction between peripheral phenyl rings perpendicular to the silole rings that prevent nonradiative energy dissipation has been proposed. On the contrary, in the *thermodynamically preferred state*, another different model for the interchain interactions has to be proposed. The model for the *thermodynamically preferred state* has to account for the volume shrinkage of the polysilole siloxane thin films, which is evident from the increase in the film density estimated in SE. This is schematically shown in Figures 8 and 13f, where the cofacial $\pi-\pi$ interaction, in a skewed manner, is enhanced with the phenyl groups perpendicular to the silole rings. The higher potential energy, accompanied with distortion of the conformational structure of the polymers, is compensated by the energy release from the $\pi-\pi$ interactions between the phenyl groups of the silole ring of the two adjacent polymer chains. The distance between the phenyl rings that can interact with each other in the *thermodynamically preferred state* is much shorter than that in the *kinetically preferred state*, which eventually affects the interchain electron transfer; this will be discussed in the capacitance—voltage ($C-V$) results below.

This *thermodynamically preferred state* has not been proposed in previous studies of silole-related molecules. This previous rareness is thought to be related to the sample preparation conditions in those studies, such that even thin films were formed by simple coating and solvent evaporation; curing conditions above 100 °C were not applied in those studies. It has been common knowledge that, for spin-on glass, tensile stress is enhanced after film curing. The induced tensile stress provokes some extension of the polymer chains in the direction parallel to substrate surface, enhancing the interchain interactions in the direction perpendicular to the substrate surface. This is a driving force to overcome an energy barrier to the *thermodynamically preferred state*.

The authors can also account for the changes in refractive index and thickness as the temperature increased above 100 °C, using the above TGA and XPS results.

- (i) 200–350 °C: Decomposition of the organic species is accelerated, consistent with the TGA results in Figure 6a and the XPS results in Figure 6d. This provides the decrease in the effective volume of the polymer chains, decreasing film thickness. Furthermore, the gradual disappearance of highly polarizable organic groups decreases the refractive index constantly.
- (ii) 100–200 °C: The additional weight loss shown in the TGA results (Figure 6a) is related to the condensation reaction of the Si—OH groups. This provides a decrease in the effective volume of the polymer chains, decreasing the film thickness. This is thought to increase the refractive index of the films within this temperature range, which is contradicted with the SE results showing its slight decrease (Figure 7b). The authors contend that the increase in the refractive index, owing to the condensation reaction, is negated by the decrease in the refractive index due to slight decomposition of the organic groups, giving rise to a

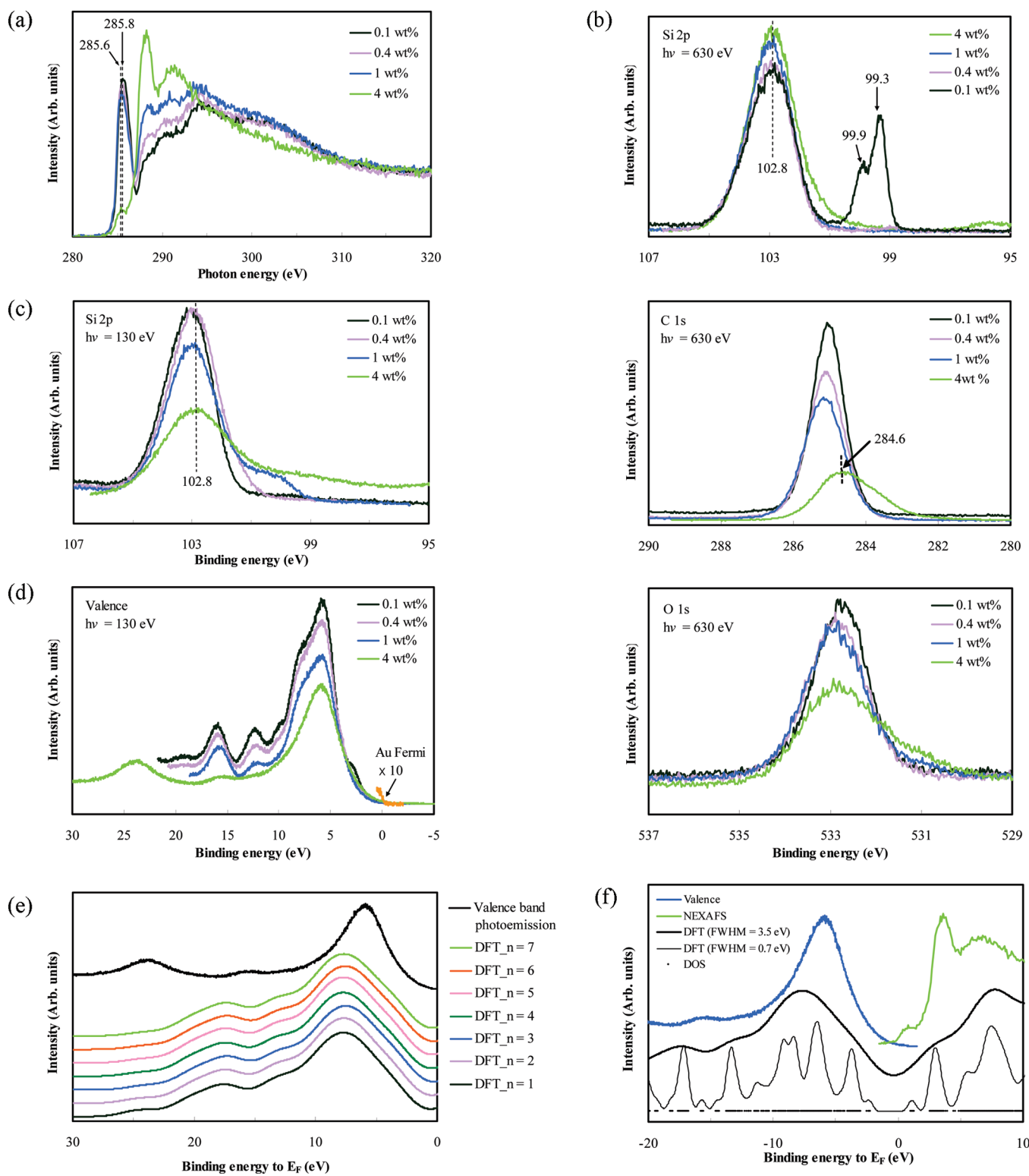


Figure 9. (a) Near-edge X-ray fine structure spectroscopy. Especially, for the poly(tetraphenyl)silole siloxane thin films fabricated from 4 wt % solution, the peak due to excitation from the C1s to LUMO level appeared at 285.6 eV. (b) Core level photoemission spectra. In the Si 2p spectra, the binding energy of the Si 2p electron in the poly(tetraphenyl)silole siloxane thin films was determined to be 102.8 eV by performing the charge calibration procedure, positioning the binding energy of the Si 2p electron of the silicon substrate to 99.3 eV. For the poly(tetraphenyl)silole siloxane thin films fabricated from 4 wt % solution, the binding energy of the C 1s electron in the poly(tetraphenyl)silole siloxane thin films was determined to be 284.6 eV. (c) Si 2p spectra for the photon energy of 130 eV. (d) Valence band photoemission spectra in the case of photon energy of 130 eV. (e) Comparison of the valence band photoemission spectrum for the 4 wt % case with the simulated spectrum ($n = 1-7$). (f) Comparison of the photoemission and the NEXAFS spectra with the simulated spectrum for occupied and unoccupied orbitals ($n = 7$).

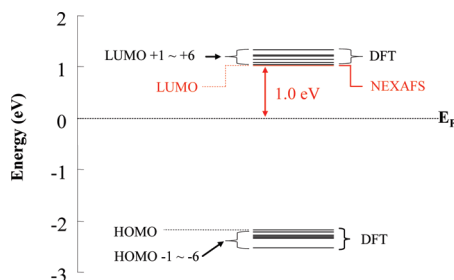


Figure 10. Energy diagram of molecular orbitals of the poly(tetraphenyl)silole siloxane with respect to the Fermi energy level (E_F). The relative position of the E_F was obtained by subtracting the C 1s peak energy (284.6 eV) in the photoemission spectra from the first absorption peak energy (285.6 eV) in the NEXAFS, from the poly(tetraphenyl)silole siloxane thin films fabricated from the 4 wt % solution. The LUMO levels were drawn from the DFT calculation results. The HOMO levels were also estimated from DFT calculation results.

slight decrease in the refractive index. Accordingly, the authors tentatively assume there is a little decomposition of the silole rings, even though this is not evidently detected in the TGA results (Figure 6a).

NEXAFS and HRPE Studies. NEXAFS is used to monitor the electronic transitions from the core level of a specific atomic species of a molecule to its unoccupied molecular orbitals (π^* and σ^* orbitals).³⁰ The transition probability of these excitations are dictated by dipole and symmetry selection rules. In this article, the focus was on determination of the LUMO energy level, which was very crucial in explaining the electron trapping mechanism in the MOS device, and will be discussed in the following subsection. The NEXAFS spectrum of the polysilole siloxane thin film near the carbon K-edge is shown in Figure 9a. For the polysilole siloxane thin film spin-coated from the 4 wt % precursor solution, a narrow peak was positioned at 285.6 eV, which was overlaid by a preband at the low-energy side and a more complex structure at higher ranges. The narrow peak was assigned to a electronic transition from the C 1s core level to the LUMO of the molecule, whose molecular orbital shape is modeled like II-11, as shown in Figure 5c. However, as discussed below in the HRPE results for core levels, the binding energy of the C 1s core level for the film fabricated from the 4 wt % precursor solution was found to be 284.6 eV, the energy difference of a C 1s core level and Fermi energy level (E_F). Since the narrow peak of 285.6 eV in the NEXAFS corresponds to an electronic transition from the C 1s core level to the LUMO, the energy of the LUMO is determined to be 1.0 eV above with respect to the E_F , as depicted in Figure 10.

In the core-level photoemission spectroscopy of the polysilole siloxane thin films using a photon energy of 630 eV (Figure 9b), the binding energies of the electrons in the Si 2p and C 1s orbitals were investigated. The first obstacle confronted was the charging problem that usually occurs in photoemission studies of an insulator. Then, the binding energy of the Si 2p electron was calibrated to a known value. As shown in the Si 2p spectrum in Figure 9b, the polysilole siloxane thin films fabricated from 0.1 wt % precursor solution showed two prominent peaks, where the former peak was due to the Si atoms in the thin films and the latter to the Si atoms of the silicon substrate, owing to its relatively low thickness. Because the binding energy of the Si 2p electrons from the silicon substrate -bulk silicon- is 99.3 eV,³¹ the latter peak was calibrated to 99.3 eV and, hence, positioned the former peak to 102.8 eV without further consideration. The

peak at 99.9 eV might arise from a Si atom at an imperfect oxidation state of +1, in the shallow native-oxide layer between the polysilole siloxane film and Si wafer.³² In addition, the Si 2p peak at 103.4 eV from the Si atom, with an oxidation state of +4 in the native oxide, might be overlapped and thus hidden by the strong peak at 102.8 eV from the polysilole siloxane thin films.

Considering the same chemical environment of the Si atoms of the other three films, the Si 2p peaks for 0.4, 1, and 4 wt % precursor solutions must also be positioned at 102.8 eV. After applying the binding energy shift values used for the charge calibrations into the C 1s and O1s spectra, this lab also obtained the charge-calibrated ones, as shown in Figure 9b.

It is possible to discuss the oxidation state of Si atoms from binding energy values. The binding energy for the Si atoms of an oxidation state of +2 is 102.1 eV, while that for the oxidation state of +3 is 102.8 eV.³³ It is interesting that the binding energy for the Si atom of the polysilole siloxane thin films is the same as that for the +3 oxidation state, since the formal charge of the silicon atom is +2. The authors speculate that this is due to the high electron affinity of the (tetraphenyl)silole ring, decreasing the electron density of the adjacent silicon atom. In a materials science sense, electron affinity (χ) is defined as the energy required to remove an electron from the bottom of the conduction (E_C), whereby $\chi = E_0 - E_C$, in which E_0 is the vacuum energy level.^{18a} The E_C of the polysilole siloxane thin films originates from the LUMO energy of the polysilole siloxane, which is discussed in the above DFT Calculations. The high electron affinity of the (tetraphenyl)silole ring, owing to the low-lying LUMO, is favorable for capturing electrons from the Fermi energy level of adjacent metal or semiconductor layers when the polysilole siloxane thin film is inserted between the metal and semiconductor layers. For the polysilole siloxane, due to the intrachain energy barrier from the –Si–O–Si– bond, the electron transferred from the Fermi energy level of the metal or semiconductor layer is trapped in the LUMO energy level of the silole group.

The important aspect of the C1s spectra is the binding energy value itself for the film fabricated from the 4 wt % precursor solution, 284.6 eV. This is because it has to be compared to the NEXAFS data, as discussed above, in order to provide the physicochemical origin for the negative charge trap properties of polysilole siloxane thin films spin-coated from the 4 wt % precursor solution. In the presented system, the high electron affinity is crucial in explaining the charge-trapping properties. The C 1s binding energy increased at the higher electron deficiency of the C atom, while the LUMO energy can be also affected by electron deficiency. Then, binding energy in XPS or charge trapping in the following capacitance–voltage (C–V) measurement could potentially be affected by electron deficiency or electron affinity. The authors surmise that the C 1s binding energy in the polysilole siloxane thin films is related to the charge trap properties.

As shown in Figure 9c, the binding energy of the Si 2p peak, in the case of 130 eV photon energy, was also charge calibrated to 102.8 eV. This calibration allows the valence level spectra obtained for the 130 eV photon energy to be charge calibrated to Figure 9d. Valence band photoemission spectroscopy was used to investigate the valence band of the molecular orbitals of the molecular solids. A broad and strong peak appeared near 6 eV, with a weak and broad peak near 16 eV. In order to investigate the origin of the valence spectrum, this lab simulated the photoemission spectra of the polysilole siloxane ($n = 1–7$) from the DFT calculation results using Gausssum software.³⁴ Then, the valence level spectrum for the 4 wt % case was compared with the simulated spectra, as shown in Figure 9e. Here, all of the simulated spectra ($n = 1–7$) were

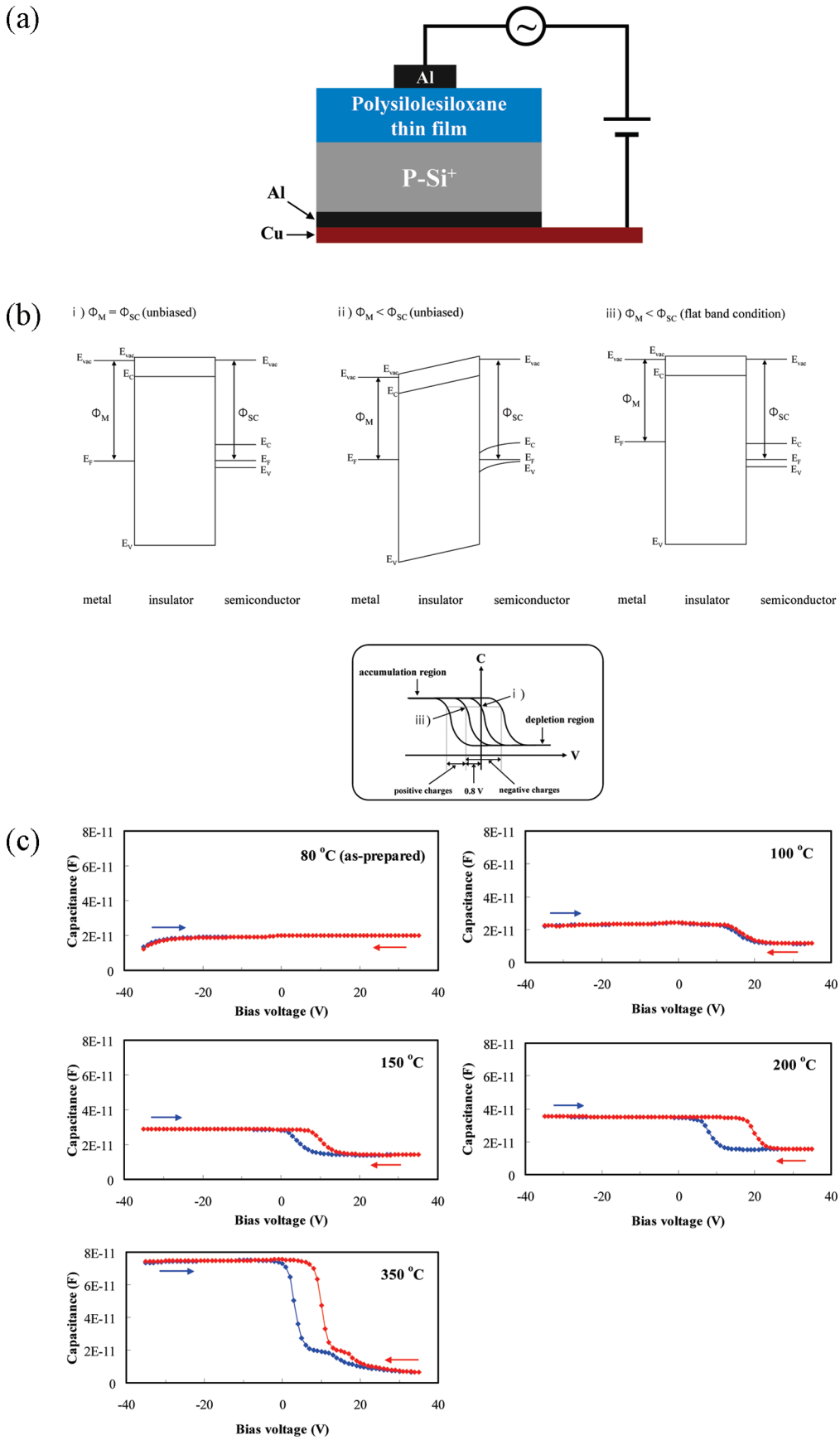


Figure 11. (a) Schematic of the vertical structure of the MIS device. (b) Energy band diagram for three typical cases. (c) Capacitance–voltage (C – V) characteristics for the poly(tetraphenyl)silole siloxane thin films according to the curing temperature.

Table 1. Thicknesses and Dielectric Constants of the Poly(tetraphenyl)silole Siloxane Thin Films (abbreviated polysilole siloxane thin films) Cured at 80, 100, 150, 200, and 350 °C^a

curing temp. (°C)	thickness (nm)	dielectric constant	reverse sweep		forward sweep	
			ΔV _{FB,2} (V)	ρ (C·cm ⁻³)	ΔV _{FB,2} (V)	ρ (C·cm ⁻³)
80	351	3.00	>35.8	>0.015	>35.8	>0.015
100	290	3.02	15.9	0.010	14.4	0.009
150	264	3.28	9.7	0.008	3.5	0.003
200	205	3.32	19.7	0.028	7.7	0.011
350	107	3.39	9.9	0.052	3.0	0.016

^a Flat band shift (ΔV_{FB,2}) due to the charges trapped over the film thickness and trap densities of negative charges (|ρ|) for reverse sweep (starting from positive bias conditions) and forward sweep (starting from negative bias conditions) directions were also summarized.

calibrated by positioning the LUMO to 1.0 eV, as mentioned in the NEXAFS results. For instance, since the band gap value (HOMO–LUMO gap) in the polysilole siloxane (*n* = 7) was estimated at 3.193 eV from the DFT calculation, the binding energy scale in the simulated valence band spectrum was calibrated to position the HOMO level to –2.193 eV, if the LUMO level was set to 1.0 eV above the *E_F*. Similar to the valence level spectrum for the 4 wt % case, the simulated spectra showed two peaks at 7 and 17 eV, with a 10 eV difference, while the shapes of the simulated photoemission spectra were nearly identical regardless of the number of (tetraphenyl)silole groups (*n*). In Figure 9f, the photoemission and NEXAFS spectra of the 4 wt % polysilole siloxane thin film are compared with the simulated spectra for occupied and unoccupied orbitals (*n* = 7). The positioning of relatively low unoccupied and high occupied orbitals is summarized in Figure 10.

Charge Trap Properties of Polysilole Siloxane Thin Films. To investigate the dielectric and charge trap properties of the polysilole siloxane thin films, capacitance–voltage (C–V) curves were obtained in typical MIS devices at which thermally deposited Al and low-doped p-type Si wafers were used as the metal and semiconductor, respectively; this is schematically illustrated in Figure 11a. A bias voltage was applied to the aluminum top electrode with respect to the silicon wafer in the MIS structures.

Under the negative bias voltage at the aluminum electrode, the holes that were major carriers in the p-type silicon wafer tended to move toward the interface between the insulator layer and the silicon wafer. This condition is called the “accumulation region” in the typical capacitance–voltage (C–V) graphs, Figure 11b. Here, the thickness of the insulator is directly used for the thickness value (*d*), and for calculating the dielectric permittivity (ϵ), as shown in the following equation:

$$C = \epsilon \epsilon_0 \frac{A}{d} \quad \epsilon_0 = 8.854 \times 10^{-12} \text{ F/m} \quad (3)$$

Conversely, in the positive bias voltage at the aluminum electrode, the holes are subjected to move down to the bulk of the silicon wafer, and the depletion layer, where the holes are deficient, is newly formed at the interface between the insulator layer and silicon wafer. This condition is referred to as the “depletion region” in the C–V graph, as shown in Figure 11b. The thickness of the depletion layer (*d_{dep}*) has to be added to calculate the dielectric permittivity, as shown in the following equation:

$$C = \epsilon \epsilon_0 \frac{A}{d + d_{\text{dep}}} \quad \epsilon_0 = 8.854 \times 10^{-12} \text{ F/m} \quad (4)$$

Although the thickness of the depletion layer and the concentration of the minor carriers (electron in p-type silicon wafer) within

it are dependent on the frequency and amplitude of the applied voltage and doping concentration of the silicon wafers, it remains difficult to determine *d_{dep}* exactly. Therefore, the capacitance in the accumulation region from eq 3 is used to calculate the dielectric permittivity in the dielectric thin films, which are shown as the flat region in the C–V graphs.

Further important information obtained from the C–V curves is the flat band shift (ΔV_{FB}). In the MIS structures, the band structure of the silicon substrate very close to the insulator is not flat, but rather bent down at the p-type semiconductor, as shown in the case of Φ_M < Φ_{SC} (unbiased) in Figure 11b; this is known as band bending. When a negative bias voltage is applied at the top electrode, the band structures at the regions become flat, as shown in the case of Φ_M < Φ_{SC} (flat band condition) in Figure 11b. In the MIS structure containing an aluminum electrode and p-type semiconductor, ΔV_{FB}, specifically ΔV_{FB,1}, is estimated to be 0.8 eV, as the Fermi energy of 4.1 eV of aluminum (Φ_M) is lower than 4.9 eV, that of the semiconductor (Φ_{SC}).³⁵

However, the presence of some charges, positive or negative, in the insulator can also change the extent of band bending. As a result, in order to render the band flat, the voltage applied at the aluminum electrode has to be different, indicating that the ΔV_{FB} value changed. Generally, the presence of positive charges shifts the ΔV_{FB} in the negative direction, while the presence of negative charges shifts the ΔV_{FB} in the positive direction.

The C–V curves for the polysilole siloxane thin films, according to the curing temperature, are shown in Figure 11c. With the capacitance in the accumulation region of the C–V curves and the thickness from the SE results, dielectric constants were calculated using eq 3, as summarized in Table 1.

It is very reasonable that, in all samples, there were only positive ΔV_{FB} values, indicating the trapping of negative charges (electrons). This is because the poly(tetraphenyl)silole siloxane dielectrics have LUMO energy levels of high electron affinity, as explained in the Introduction and the NEXAFS results. Even in the as-prepared sample (80 °C) showing only a flat curve, it is evident that its ΔV_{FB,tot} (total flat band shift) is greater than 35 V. This is because their capacitance value was surely due to the accumulation region, as compared to that for 100 °C. From the ΔV_{FB,tot} values of these graphs, the volume densities of trapped charges (ρ; charge trap density) are calculated using eqs 5–9:^{18b} The ΔV_{FB,tot} is divided into four specific terms:

$$\Delta V_{\text{FB,tot}} = \Delta V_{\text{FB},1} + \Delta V_{\text{FB},2} + \Delta V_{\text{FB},3} + \Delta V_{\text{FB},4} \quad (5)$$

where ΔV_{FB,1} is due to the work function difference of the aluminum and silicon substrates, which was estimated to be –0.8 eV, as explained above. The value ΔV_{FB,2} is due to the charges

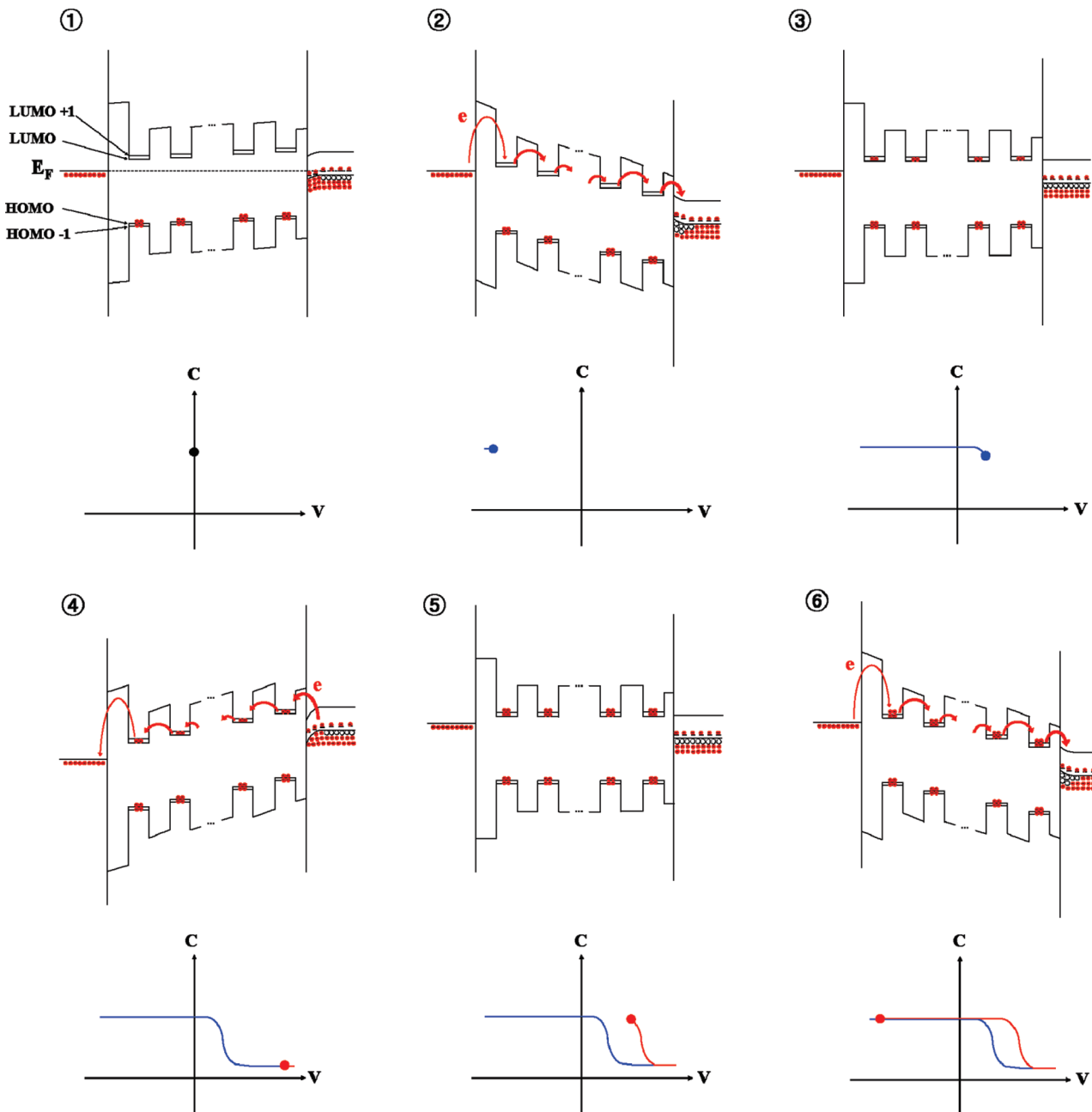


Figure 12. Representation of the step potential model in the energy diagrams of the MIS device, explaining the C–V hysteresis phenomena. At a negative bias, the electron is injected from the aluminum electrode into the poly(tetraphenyl)silole siloxane thin film, inducing a positive flat band shift (ΔV_{FB}). At a positive bias condition, the electron is injected from the silicon substrate, inducing a more positive flat band shift (ΔV_{FB}).

trapped over the film thickness, $\Delta V_{FB,3}$ and $\Delta V_{FB,4}$ are due to structural defects in the silicon during oxidation and interface-trapped charges, respectively, and $\Delta V_{FB,3}$ and $\Delta V_{FB,4}$ are tentatively assumed to be very small. Thus:

$$\Delta V_{FB,2} = \Delta V_{FB,\text{tot}} + 0.8 \text{ V} \quad (6)$$

The relationship between $\Delta V_{FB,2}$ and the negative charge trap density (ρ) has to be considered as follows, where t is film thickness:

$$\Delta V_{FB,2} = - \int_0^t \frac{\rho(x) \cdot x \cdot dx}{\epsilon_0 \cdot \epsilon_{OX}} \quad (7)$$

Here, $\rho(x)$ is also assumed to be uniform according to x , along the film depth, $\rho(x) = \rho$:

$$\Delta V_{FB,2} = - \frac{\rho}{\epsilon_0 \cdot \epsilon_{OX}} \int_0^t x dx = - \frac{\rho}{\epsilon_0 \cdot \epsilon_{OX}} \frac{1}{2} t^2 \quad (8)$$

Thus, the trap density of negative charges ($|\rho|$) is estimated from $\Delta V_{FB,2}$:

$$|\rho| = \frac{2\epsilon_0 \cdot \epsilon_{OX}}{t^2} (\Delta V_{FB,2}) \quad (9)$$

In both cases of reverse and forward sweep directions, the

estimated charge trap densities for the negative charges are summarized in Table 1. In the low curing temperature ranges of up to 150 °C, the trap density of negative charges ($|\rho|$) decreased as the curing temperature increased. The authors hold that this is related to the changes in the nanoscopic arrangement of the polymer chains according to curing temperature. As illustrated in Figure 8a, the *thermodynamically preferred state* becomes dominant at relatively higher curing temperatures, within a range of up to 150 °C, where the cross section of the cofacial $\pi-\pi$ interaction in the nearest phenyl rings is greatly enhanced. In this nanoscopic arrangement, the interchain electron transfer rate increased, provoking a decrease in the trap density of the negative charges ($|\rho|$), which will be qualitatively explained in the following subsection.

Within high curing temperature ranges above 150 °C, the trap density of negative charges ($|\rho|$) increased as the curing temperature increased, as shown in Table 1. This is thought to be related to the formation of a new charge trap center due to the thermal decomposition of the (tetraphenyl)silole rings in the polymer chains, mentioned in the above TGA and FT-IR results.

The appearance of the positive flat band shift is more succinctly explained by modifying the step potential model in Figure 5d and applying the molecular orbital energy diagram discussed in Figure 10 toward the electronic energy diagram of the MIS structure, as shown in Figure 12. This model is to be restrictively applied toward only the samples cured at low temperature ranges (≤ 150 °C), with no thermal decomposition of the (tetraphenyl)silole rings. Here, the energy barriers of the interchain electron transfer were displayed, instead of those of the intrachain electron transfer. For the simplification, electron energy levels displayed within energy barriers were taken from only few energy levels of HOMO, HOMO + 1, LUMO, and LUMO + 1. The relative proximity of the LUMOs to E_F in terms of electronic energy, compared to HOMOs, resulted in the phenomenological situation whereby the electron is the owner of the charge trapping of the polysilole siloxane dielectric thin films, rather than the hole.

At negative bias condition ②, electrons from the metal electrodes are injected into the LUMO level of the polymer through a tunneling mechanism. These electrons are transported to unoccupied molecular orbitals or vibronically excited states of the LUMO level of another adjacent polymer through a resonant-tunneling mechanism, which are electronically or vibrationally de-excited into the LUMO level within a very short time. The interchain electron transfer enables the electrons to reach the polymer next to the silicon substrate, where the electron is transported into the conduction band of the p-type silicon. This progressing electron transport through the poly(tetraphenyl)silole siloxane dielectrics maintains the steady-state condition of the charge density within the unit volume. When the negative bias condition is turned off, some of the electrons are stored in the dielectrics, noted as *electron trapping*, generating the positive flat band shift, as illustrated at ③ and ④ in Figure 12.

At positive bias condition ④, the electron transport and trapping proceed in a reversed manner. The electrons in the doping level and the topmost energy levels of the valence band in the depletion region are injected into the LUMO level

of the polymer through a tunneling mechanism. These electrons are also transported to unoccupied molecular orbitals or vibronically excited states of the LUMO level of the adjacent polymer through a resonant-tunneling mechanism, which are electronically or vibrationally de-excited into the LUMO level within a very short time. The inter-chain electron transfer continues in order for the electrons to reach the polymer next to the aluminum metal, where the electron is transported into the Fermi energy level of the aluminum.

The origin of the anticlockwise C–V hysteresis over the entire curing temperature range is related to why the electron trapping in the reverse sweep condition (positive bias condition, ④) is higher than that in the forward sweep condition (negative bias condition, ②), which is confirmed by comparison of the trap density of negative charges ($|\rho|$) in Table 1. The authors propose that this is attributed to formation of an additional conducting channel between the polymer and native SiO₂ of approximately 15 Å on the silicon substrate. The Si–O–Si linkage is formed from the terminal Si–OH of the polymer chain; the Si–OH's existed on the native oxide. Tunneling through the σ bond is known to be much faster than through space.^{36,37} The higher $|\rho|$ values for the reverse sweep conditions, compared with forward sweep conditions, is due to the fast electron pumping from the silicon substrate to the polymer dielectrics thin film via electron tunneling through the σ bond (Supporting Information, Remarks S1). This is why a relatively low-energy barrier at the interface of the polymer dielectric and silicon substrate is displayed in the electronic energy diagram of the MIS structure, as shown in Figure 12. This trend is much more strengthened as the curing temperature is increased. This is certainly because the Si–OH condensation reaction forming the interfacial Si–O–Si linkages is more promoted at higher curing temperatures.

Schematic Demonstration for the Negative Charge Trapping in the Poly Tetraphenylsilole Siloxane for Samples Cured at Low Temperature Ranges (≤ 150 °C). This interpretation mainly focuses on the explanation of the $\Delta V_{FB,2}$ and $|\rho|$ values in the **forward sweep direction** for the samples cured at low temperature ranges (≤ 150 °C), whereby the electron trapping and electron transfer phenomena were found to be more closely related. This also enabled the authors to recognize that investigation of the electron tunneling process between the adjacent π organic groups was very important for understanding the electron transfer kinetics of polymers having quantum well structures. The similar demonstration for the **reverse sweep direction** was summarized separately (Supporting Information Figure S4), clarifying the interfacial Si–O–Si linkages to explain the anticlockwise C–V hysteresis.

In the interpretation of C–V results of the above subsection, the charge density (ρ) was held constant over the film thickness. This was based on the following evident arguments for the kinetics regarding electron transfer and trapping. The simple model of the kinetics is proposed in Figure 13a. Here, the dielectrics layer is treated with a series of volume elements, the number of which is n , and whose area is A , and thickness is approximately t/n . The values $\rho_{f,n}$, ρ_m , and ρ_s respectively denote the negative charge trap density for each element at negative bias condition, metal, semiconductor, while k_m , k_1 , k_2 , ..., k_{n-1} ,

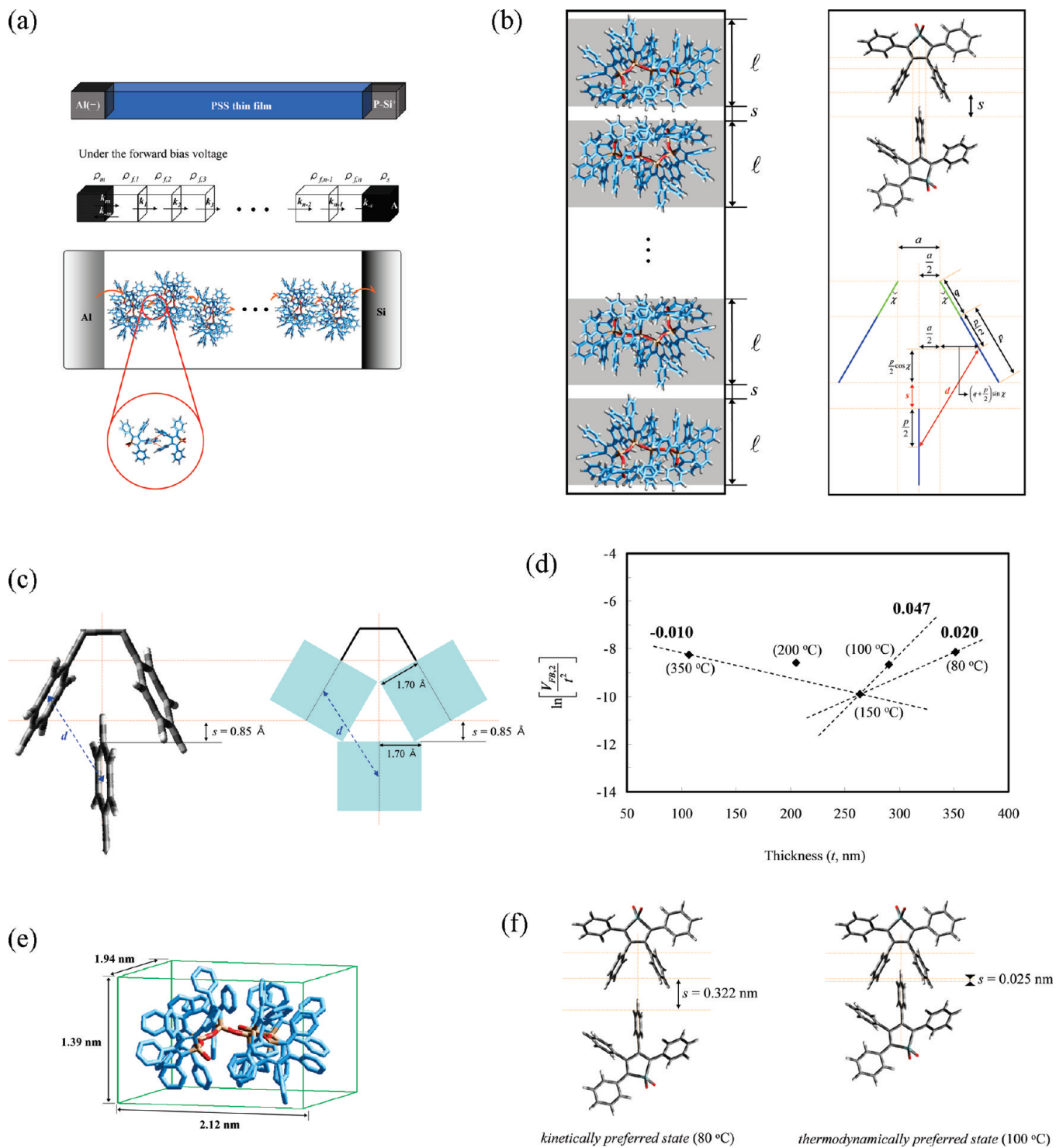


Figure 13. Origin of interchain electron transfer. (a) An electron transfer kinetics model at a negative bias voltage for the forward sweep direction (b) Geometric details for describing the cofacial interaction in a skewed manner of two phenyl rings at the interfaces of the adjacent polymer chains (c) The model of the intermolecular interaction considering van der Waals thickness of the phenyl rings (d) Logarithmic relation of ΔV_{FB} and thickness (e) The optimized geometry of the polymer ($n = 7$) obtained using DFT calculations with Gaussian03 were applied for packing the volume between the aluminum and silicon parts. (f) The changes in the interchain distance (s) and the distance of the phenyl rings (d) at the interface of the polymer chains for the *kinetically preferred state* and *thermodynamically preferred state*.

and k_s are the rate constants for electron transfer in the direction for the aluminum to silicon substrate under negative bias conditions.

Forward Sweep Direction Case. Under negative bias conditions, for the first element, the steady-state approximation for the charge trap density of the first element ($\rho_{f,1}$)

is applied:



$$\frac{d\rho_{f,1}}{dt} = k_m \rho_m - k_{-m} \rho_{f,1} - k_1 \rho_{f,1} = 0 \quad (11)$$

$$\rho_{f,1} = \frac{k_m}{k_{-m} + k_1} \rho_m \quad (12)$$

Without any evidence, the electron transfer rate inside the poly(tetraphenyl)silole siloxane dielectrics is assumed to be higher than that from the polymer dielectrics to the aluminum electrode, $k_1 \gg k_{-m}$:

$$\rho_{f,1} = \frac{k_m}{k_1} \rho_m \quad (13)$$

For the second element:



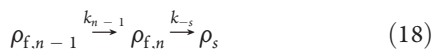
$$\frac{d\rho_{f,2}}{dt} = k_1 \rho_{f,1} - k_2 \rho_{f,2} = 0 \quad (15)$$

$$\rho_{f,2} = \frac{k_1}{k_2} \rho_{f,1} \quad (16)$$

Assuming that the rate constants for the electron transfer over all volume elements inside the polysilole siloxane dielectrics are the same ($k_1 = k_2 = \dots = k_{n-1}$):

$$\rho_{f,2} = \rho_{f,1} \quad (17)$$

As a result of the above assumptions, the volume densities of the negative charges for all elements are also the same ($\rho_{f,1} = \rho_{f,2} = \rho_{f,3} = \dots = \rho_{f,n-1}$), except for the n th element, which was located next to the silicon substrate. For the n th element:



$$\frac{d\rho_{f,n}}{dt} = k_{n-1} \rho_{f,n-1} - k_{-s} \rho_{f,n} = 0 \quad (19)$$

$$\rho_{f,n} = \frac{k_{n-1}}{k_{-s}} \rho_{f,n-1} \quad (20)$$

As mentioned earlier, there are certainly Si—O—Si linkages at the interface between the (tetraphenyl)silole siloxane polymer dielectrics and the silicon substrate, resulting in higher electron transfer rates than those between π organic groups, $k_{-s} \gg k^{n-1}$. Accordingly:

$$\rho_{f,n} \rightarrow 0 \quad (21)$$

Overall:

$$\rho_f \equiv \rho_{f,1} = \rho_{f,2} = \rho_{f,3} = \dots = \rho_{f,n-1} = \frac{k_m}{k_1} \rho_m \quad (22)$$

Equation 8 is modified for a forward sweep direction:

$$\Delta V_{FB,2}^f \cong -\frac{\rho_f}{\epsilon_0 \cdot \epsilon_{OX}} \frac{1}{2} t^2 \quad (23)$$

$$\Delta V_{FB,2}^f \cong -\frac{1}{k_1} \frac{k_m \cdot \rho_m}{\epsilon_0 \cdot \epsilon_{OX}} \frac{1}{2} t^2 = C \cdot \frac{1}{k_1} \cdot t^2 \quad (24)$$

The rate constant for the electron transfer inside the polysilole siloxane dielectrics (k_1) is surely thought to originate from the interchain electron transfer rate of the poly(tetraphenyl)silole siloxane polymer chains. This interchain electron transfer occurs thorough electron tunneling through the two nearest (tetraphenyl)silole rings, which is classified into as electron transfer through space and whose rate constants have been known to exponentially decay.^{23,36,37} Then, with a proportion constant α :

$$k_1 = \alpha \cdot e^{-\beta \cdot d} \quad (25)$$

$$\Delta V_{FB,2}^f = C \cdot \frac{1}{\alpha \cdot e^{-\beta \cdot d}} t^2 \quad (26)$$

where d is surely the interdistance between phenyl rings on the silole rings:

$$\frac{\Delta V_{FB,2}^f}{t^2} = C \cdot \alpha^{-1} \cdot e^{\beta \cdot d} \quad (27)$$

Nonetheless, collection of the n volumes arranged perpendicular to the substrate surface through the dielectric films are modeled as shown in Figure 13b, where $/$ is volume height, perpendicular to the substrate surface, and s the distance between the volumes in the same direction, in which the number of C atoms is considered. Here, “a volume” denotes a three-dimensional, hypothetical box containing a poly(tetraphenyl)silole siloxane chain.

$$t = n/ + (n-1)s \cong n/ + ns \quad (28)$$

$$s = \frac{t}{n} - / \quad (29)$$

In Figure 13b, even though each volume element is tentatively depicted by a polymer chain, this is not yet confirmed. As shown again in Figure 13b, assuming that the interface between the volume elements consists of the interactions of the peripheral phenyl rings, the geometrical relationship between d and s can be derived:

$$d = \sqrt{s(s + p + p \cos \chi) + C'} \quad$$

$$d = \sqrt{s(s + p + p \cos \chi) + C'} \left(C' = q(q + p) \sin^2 \chi + a \left(q + \frac{p}{2} \right) \sin \chi + \frac{p^2}{2} \cos \chi + \frac{1}{2} \left(p^2 + \frac{a^2}{2} \right) \right) \quad (30)$$

As shown in Figure 13c, if half (1.70 Å) of the van der Waals thickness of the waiting phenyl groups is considered,³⁸ the minimal value of s is estimated to be approximately 0.85 Å. From the previous report on benzene–benzene interaction, the edge-to-face type configuration allows for a shorter intermolecular distance by approximately 0.40 Å, compared with that obtained using a van der Waals thickness (2.50 Å versus 2.90 Å).³⁸ In addition, it was also reported for benzene dimer that the intermolecular interaction potential energies were calculated to be the largest (most negative) when the intermolecular distances were approximately 3.79 and 5.00 Å for the T-shaped and the parallel structures, respectively.²⁸ Therefore, the intermolecular distance (d) between the phenyl groups of the silole ring and the approaching phenyl ring shown in Figure 13c would be in the

Table 2. In the Low Curing Temperature Ranges (≤ 150 °C), the Interchain Distance (s) and the Interdistance (d) of Phenyl Rings, Defined in Figure 13b, were Estimated Using $s = (t)/(n) - \ell$ and $d = 0.835s + 0.346$ (nm), respectively^a

temp. (°C)	t (nm)	$(t)/(205)$ (nm)	$s (d)$ (nm)			
			$n = 6$		$n = 7$	
			DFT ($\ell = 1.37$)	PM3 ($\ell = 1.33$)	DFT ($\ell = 1.39$)	PM3 ($\ell = 1.24$)
80	351	1.712	0.342 (0.643)	0.382 (0.681)	0.322 (0.624)	0.472 (0.767)
100	290	1.415	0.045 (0.378)	0.085 (0.411)	0.025 (0.362)	0.175 (0.490)
150	264	1.288	-0.082 (0.285)	-0.042 (0.312)	-0.102 (0.273)	0.048 (0.381)
						-0.012 (0.334)

^a The height (ℓ) of a polymer chain was measured from the optimized geometry obtained from the DFT calculations, as shown in Figure 13e.

range of 3.79–5.00 Å corresponding to the s values of 0.48–1.87 Å calculated by eq 30 (Supporting Information Figure S5), respectively. Then, the s is tentatively assumed to decrease further to approximately −0.1 nm. The maximal value of s is set to 0.2 nm, which is thought to be sufficient for investigating the intermolecular interaction of the phenyl rings.

In the range of -0.100 nm $< s < 0.200$ nm (Supporting Information Figure S5):

$$d \cong 0.803s + 0.346 \text{ (nm)} \quad (31)$$

Substituting eq 29 into eq 31:

$$d \cong 0.803\left(\frac{t}{n} - \ell\right) + 0.346 \quad (32)$$

Substituting eq 32 into eq 27 and taking the logarithm:

$$\ln\left[\frac{\Delta V_{FB,2}^f}{t^2}\right] = \ln(C \cdot \alpha^{-1}) + \beta \cdot d \quad (33)$$

$$\ln\left[\frac{\Delta V_{FB,2}^f}{t^2}\right] \cong \ln(C \cdot \alpha^{-1}) + \beta \cdot 0.803\left(\frac{t}{n} - \ell\right) + 0.346 \quad (34)$$

$$\ln\left[\frac{\Delta V_{FB,2}^f}{t^2}\right] \cong [\ln(C \cdot \alpha^{-1}) - 0.803\beta \cdot \ell + 0.346] + \frac{0.803 \cdot \beta}{n} t \quad (35)$$

As shown in Figure 13d, $\ln[(\Delta V_{FB,2}^f)/(t^2)]$ is plotted according to the film thickness (t), which is compared to eq 35. From this graph, $(0.803 \cdot \beta)/(n)$ was estimated to be 0.047 – 0.020 nm^{−1} in the low-temperature ranges. As mentioned in the C–V results, the $\Delta V_{FB,2}$ for the 80 °C-cured sample was undervalued, confirming only the lower limit, because the accumulation region in the C–V graphs swept over the entire sweep voltages. Then, it is thought to be more reasonable to take the tentative $(0.803 \cdot \beta)/(n)$ value (0.047) from the $\Delta V_{FB,2}$ values for the 100 and 150 °C-cured samples.

The theoretical calculation of decay constant β for electron tunneling between the interchains has not yet been executed. However, the authors tentatively muse that the tunneling process occurs between the (tetraphenyl)silole rings. More specifically, the process involved the phenyl rings accompanying cofacial π – π interactions. Fortunately, in recent years, the β value for electron tunneling through phenyl rings was determined to be near 12 nm^{−1} from a luminescence decay kinetics experiment.^{36,37} Using the β value, for $(0.803 \cdot \beta)/(n) = 0.047$, the number of

volume elements stacked into the vertical direction of the films (n) is estimated to be approximately 205. This implies that the total height $((t)/(n))$ of a volume element and the interchain distance to the vertical direction of the film is approximately 1.29 nm for the 150 °C-cured samples, as summarized in Table 2. This is close to the effective height of the polymer (ℓ , approximately 1.39 nm) estimated from the optimized geometry using the DFT calculations for the molecular structure of the poly(tetraphenyl)silole siloxane polymer ($n = 7$), as shown in Figure 13e. Then, very naturally, each of the volume elements was found to be occupied by a polymer chain of $n = 7$. Using eqs 29 and 32, the s and d values were also estimated for the 80, 100, and 150 °C cases, as summarized in Table 2. For the case of 80 °C, depicted as the *kinetically preferred state*, the s and d values were estimated to be 0.32 and 0.62 nm, respectively, while for the case of 100 °C, corresponding to the *thermodynamically preferred state*, they decreased to 0.025 and 0.362 nm, as shown in Figure 13f. In the latter case, the molecular orbitals of the two phenyl rings are thought to overlap each other, since the s value (0.025 nm) is slightly lower than (0.085 nm) the van der Waals contact (Figure 13c). In the case of 150 °C, the s and d values were further decreased to −0.102 and 0.273 nm, respectively, preferring the *thermodynamically preferred state*.

Nevertheless, the distance decay constant for electron tunneling β is given by the effective barrier height (ΔE_{eff}), through which electron tunneling proceeds:³⁹

$$\beta = (10.25 \text{ nm}^{-1} \text{ eV}^{-1/2}) \sqrt{\Delta E_{\text{eff}}} \quad (36)$$

Then, ΔE_{eff} is estimated to be approximately 1.4 eV, somewhat close to 1.646–1.963 eV, as the energy difference between the energy levels of the LUMO orbitals and vacuum level proposed in the step potential model of Figure Sd. This is consistent with the argument that the cofacial π – π interactions between the peripheral phenyl rings are mainly responsible for the interchain electron tunneling.

The driving force for this investigation initially came from whether the poly(tetraphenyl)silole siloxane polymer really shows the negative charge trapping phenomena as the authors planned and designed after being motivated by its low-lying LUMO orbital. The positive flat band shift (ΔV_{FB}) in the C–V graphs evidently proved that the presented design concept is working. It became apparent that investigation of the relationship between the macroscopic and microscopic properties was very important for understanding the electronic and optical properties of this kind of molecular solids. As discussed in the above subsections, the changes in intermolecular distances of the phenyl groups of adjacent polymer chains generated the variation in the electron transfer rate between them, resulting in the

alteration of electron trapping of the silole rings. The concept of quantum well structures was very useful to interpret the electron trapping phenomena, wherein the intrachain energy barriers play as an origin of the charge trapping and the interchain energy barriers act as critical factors to control the electron transfer. The authors therefore proffer that further experimental and theoretical studies are needed to understand more concretely the electron behavior of this kind of dielectrics that consists of the polymer chains of the quantum well structures.

SUMMARY

In this article, the authors present the first results of compelling research centered upon negative charge trapping and investigation of its physicochemical origin in synthesized poly(tetraphenyl)silole siloxane thin films. This lab has investigated the charge trap properties of siloxane-based dielectrics for a solution-processed floating gate layer or nanodot layer in the OTFT-based nonvolatile memory devices, where the phase problem and the lacking engineering capabilities were found. Then, a new material architecture combining the insulating properties of polyorganosiloxanes and the charge trap properties of π -conjugated organic moieties was adopted, where the two components were linked through direct chemical bonds. This is thought to prevent the phase separation problem and allow for ease of engineering of the charge trap properties. Through comprehensive discussions and analysis, the novel hybridized polymer, poly(tetraphenyl)silole siloxane, has been designed, synthesized, and characterized for the first time. For a low-lying LUMO of the silole (silacyclopentadiene) ring used as a charge-trapping center, the low-lying LUMO was thought to facilitate electron capture from the Fermi energy level of the adjacent metal and semiconductor layers. Then, in the case of using dielectrics containing the silole moiety, substantial electron trapping enhancement was expected. The negative charge trapping behavior was experimentally validated from the positive flat band shift (ΔV_{FB}) in the capacitance–voltage (C – V) characteristics in a MIS device. In order to interpret the results, the authors adopted the view of electron theory. Investigation of the molecular orbitals using DFT calculations was first performed on the polymer, instead of using the band theory, since the polymer dielectrics for the MIS device consists of molecular solids. The energy level of the LUMO was determined to be 1.0 eV above the E_F , using NEXAFS and core level photoemission spectroscopy, implying a high electron affinity. This is consistent with the electron trapping in the MIS device. The abrupt increase in the refractive index for the 100 °C-cured polysilole siloxane thin film pointed toward the nanoscopic arrangement of the polymer chains in the condensed phase. Through inexorable investigation about its origin, surprisingly, the negative charge trapping of the polysilole siloxane dielectric thin films was closely related to the electron transfer rate between the adjacent silole rings. Thus, the assertion followed that as curing temperature is increased, a phenyl group of a silole ring in a polymer chain inserts deeper into the two waiting phenyl groups of another silole ring in another polymer chain, enhancing the electron transfer between the rings. Moreover, the authors expected that the distance between the phenyl groups is within a range of 0.27–0.36 nm for the *thermodynamically preferred state*, resulting in the high refractive index. Through this demonstration, a kinetics model was needed to explain electron transfer through the dielectrics, which will surely be established as part of the electron dynamics of the molecular solids.

ASSOCIATED CONTENT

S Supporting Information. Figure S1 (GPC results), Figure S2 (^1H - and ^{13}C NMR results), Figure S3 (demonstration of proportional relationship between refractive index (n) and density (N) of films), Figure S4 (schematic demonstration for the charge trapping in reverse sweep direction), Figure S5 (plot of distance between phenyl rings (d) versus interchain distance (s)), Remark S1, and complete refs 16b and 20. This material is available free of charge via the Internet at <http://pubs.acs.org>.

AUTHOR INFORMATION

Corresponding Author

hdjeong@chonnam.ac.kr; hsohn@chosun.ac.kr

ACKNOWLEDGMENT

This research was supported by the Basic Science Research Program through the National Research Foundation of Korea (NRF) funded by the Ministry of Education, Science and Technology (No. 2010-0008824). This work was also supported by the PLSI supercomputing resources of KISTI (Korea Institute of Science and Technology Information). The experiments at the PLS were supported in part by MEST and POSTECH.

REFERENCES

- (1) Sanchez, C.; Lebeau, B. *Mater. Res. Soc. Bull.* **2001**, *26*, 377.
- (2) Sanchez, C.; Lebeau, B.; Chaput, F.; Boilot, J. P. *Adv. Mater.* **2003**, *23*, 1969.
- (3) Mitzi, D. B. *Chem. Mater.* **2001**, *13*, 3283.
- (4) Chujo, Y.; Saegusa, T. *Adv. Polym. Sci.* **1992**, *100*, 11.
- (5) Sanchez, C.; Ribot, F. *New J. Chem.* **1994**, *18*, 1007.
- (6) Böttcher, C. J. F. *Theory of Electric Polarisation*; Elsevier Publishing Company: Netherlands, 1952; p171–291.
- (7) Waser, R. *Nanoelectronics and Information Technology*, 2nd ed.; Wiley-VCH: Germany, 2005; p 36.
- (8) Kim, C. S.; Jeong, H. D. *J. Phys. Chem. B* **2008**, *112*, 16257.
- (9) Choi, J. K.; Lee, D. H.; Rhee, S. K.; Jeong, H. D. *J. Phys. Chem. C* **2010**, *114*, 14233.
- (10) (a) Jeong, H. D.; Shin, H. J.; Seon, J. B. Porphyrin Derivative for Preparing Xerogel Thin Film Which is used as Channel Material Capable of Storing Multi-Level Data in Memory Device and Method for Preparing Porphyrin Xerogel Thin Film by Using the Same. KR Patent 10-2007-0075172, 2007. (b) Jeong, H. D.; Shin, H. J.; Seon, J. B. Porphyrin-Embedded SiOC Thin Film Utilized as Charge Trapping Material and Semiconductor Channel Material, and Method for Preparing The Same. KR Patent 10-2007-0078894, 2007.
- (11) Lee, D. H.; Jeong, H. D. *J. Phys. Chem. C* **2008**, *112*, 16984.
- (12) Baeg, K. J.; noh, Y. Y.; Ghim, J.; Kang, S. J.; Lee, H. M.; Kim, D. Y. *Adv. Mater.* **2006**, *18*, 3179.
- (13) Gelinck *Nature* **2007**, *445*, 268.
- (14) Leong, W. L.; Lee, P. S.; Lohani, A.; Lam, Y. M.; Chen, T.; Zhang, S.; Dodabalapur, A.; Mhaisalkar, S. G. *Adv. Mater.* **2008**, *20*, 2325.
- (15) Kim, S. J.; Lee, J. S. *Nano Lett.* **2010**, *10*, 2884.
- (16) (a) Wakai, M.; Kobayashi, M.; Kumise, T.; Yamaguchi, M.; Nakanishi, T.; Tanaka, H. *Non-Volatile Semiconductor Memory Workshop, 2006. IEEE NVSMW 2006. 21st* **2006**, 58–59. (b) Tiwari, S.; Rana, F.; Hanafi, H.; Hartstein, A.; Crabbé, E. F. *Appl. Phys. Lett.* **1996**, *68*, 1377. (c) De Salvo, B.; *IEDM Tech. Dig.* **2003**, 597–600. (d) Lee, C.; Gorur-Seetharam, A.; Kan, E. *IEDM Tech. Dig.* **2003**, 557–560.
- (17) (a) Yamaguchi, Y. *Synth. Met.* **1996**, *82*, 149. (b) Xu, Y.; Fujino, T.; Naito, H.; Dohmaru, T.; Oka, K.; Sohn, H.; West, R. *Jpn. J. Appl. Phys.* **1999**, *38*, 6915.

- (18) (a) Sze, S. M.; Ng, K. K. *Physics of Semiconductor Devices*, 3rd ed.; John Wiley & Sons, Inc.: Hoboken, NJ, 2007; p 125, p 197.
(b) Barbottin, G.; Vapaille, A. *Instabilities in Silicon Devices: Silicon Passivation and Related Instabilities*; Elsevier Science Publishers B.V.: Amsterdam, 1991; Vol 1, pp 215–262.
- (19) West, R.; Sohn, H.; Powell, D. R.; Muller, T.; Apeloig, Y. *Angew. Chem., Int. Ed. Engl.* **1996**, *35*, 1002.
- (20) Frisch, M.; *Gaussian03*; Gaussian Inc.: Wallingford, CT, 2005.
- (21) Hummel, R. E. *Electronic Properties of Materials*, 2nd ed.; Springer-Verlag: Heidelberg, 1992; p 3.
- (22) Yu, G.; Yin, S.; Chen, J.; Xu, X.; Sun, X.; Ma, D.; Zhan, X.; Peng, Q.; Shuai, Z.; Tang, B.; Zhu, D.; Fang, W.; Luo, Y. *J. Am. Chem. Soc.* **2005**, *127*, 6335.
- (23) Kuhn, H.; Försterling, H. D.; Waldeck, D. H. *Principles of Physical Chemistry*, 2nd ed.; John Wiley & Sons, Inc.: Hoboken, NJ, 2009; p 193, p 930.
- (24) Pavia, D. L.; Lampman, G. M.; Kriz, G. S.; Vyvyan, J. R. *Introduction to Spectroscopy*, 4th ed.; Brooks/Cole: Belmont, CA, 1996; p 56.
- (25) (a) Grill, A.; Neumayer, D. A. *J. Appl. Phys.* **2003**, *94*, 6697.
(b) Lenza, R. F. S.; Vasconcelos, W. L. *Mater. Res.* **2001**, *4*, 189.
- (26) Ou, D. L.; Seddon, A. B. *J. Non-Cryst. Solids* **1997**, *210*, 187.
- (27) Donley, C. L.; Zaumseil, J.; Andreasen, J. W.; Nielsen, M. M.; Sirringhaus, H.; Friend, R. H.; Kim, J. S. *J. Am. Chem. Soc.* **2005**, *127*, 12890.
- (28) Tuzuki, S.; Honda, K.; Uchimaru, T.; Mikami, M.; Tanabe, K. *J. Am. Chem. Soc.* **2002**, *124*, 104.
- (29) (a) Levitsky, I. A.; Kim, J.; Swager, T. M. *J. Am. Chem. Soc.* **1999**, *121*, 1466. (b) Chen, J.; Law, C. C. W.; Lam, J. W. Y.; Dong, Y.; Lo, S. M. F.; Williams, I. D.; Zhu, D.; Tang, B. Z. *Chem. Mater.* **2003**, *15*, 1535. (c) Ren, Y.; Lam, J. W. Y.; Dong, Y.; Tang, B. Z.; Wong, K. S. *J. Phys. Chem. B* **2005**, *109*, 1135. (d) Tang, B. Z.; Zhan, X.; Yu, G.; Lee, P. P. S.; Liu, Y.; Zhu, D. *J. Mater. Chem.* **2001**, *11*, 2974. (e) Zhao, Z.; Chen, S.; Lam, J. W. Y.; Jim, C. K. W.; Chan, C. Y. K.; Wang, Z.; Lu, P.; Deng, C.; Kwok, H. S.; Ma, Y.; Tang, B. Z. *J. Phys. Chem. C* **2010**, *114*, 7964. (f) Yu, D.; Zhang, Q.; Wu, C.; Wang, Y.; Peng, L.; Zhang, D.; Li, Z.; Wang, Y. *J. Phys. Chem. B* **2010**, *114*, 8934.
- (30) (a) Felicissimo, V. C.; Cesar, A.; Luo, Y.; Gel'mukhanov, F.; Argen, H. *J. Phys. Chem. A* **2005**, *109*, 7385. (b) Otero, E.; Wilks, R. G.; Reiger, T.; Blyth, R. I. R.; Moewes, A.; Urquhart, S. G. *J. Phys. Chem. A* **2008**, *112*, 624. (c) Stöhr, J. *NEXAFS Spectroscopy*; Springer: New York, 1992.
- (31) (a) Norderg, R.; Brecht, H.; Albridge, R. G.; Fahlman, A.; Wazer, J. R. V. *Inorg. Chem.* **1970**, *9*, 2469. (b) Kurosawa, K.; Takigawa, Y.; Sasaki, W.; Katto, M.; Inoue, Y. *J. Appl. Phys.* **1991**, *30*, 3219.
- (32) Hirayama, H.; Watanabe, K. *Phys. Rev. B* **1995**, *51*, 14717.
- (33) Alexander, M. R.; Short, R. D.; Jones, F. R.; Michaeli, W.; Blomfield, C. *J. Appl. Surf. Sci.* **1999**, *137*, 179.
- (34) O'Boyle, N. M.; Vos, J. G. *GaussSum*; version 1.05; Dublin City University: Dublin, Ireland, 2005; available at <http://gausssum.sourceforge.net>.
- (35) Yang, E. S. *Microelectronic Devices*, International ed.; McGraw-Hill Book Co.: Singapore, 1988; p 240.
- (36) Wenger, O. S.; Leigh, B. S.; Villahermosa, R. M.; Gray, H. B.; Winkler, J. R. *Science* **2005**, *307*, 99.
- (37) Ponce, A.; Gray, H. B.; Winkler, J. B. *J. Am. Chem. Soc.* **2000**, *122*, 8187.
- (38) Endo, T.; Iida, T.; Furuya, N.; Yamada, Y.; Ito, M. M. *J. Chem. Software* **1999**, *5*, 81.
- (39) Skourtis, S. S.; Beratan, D. N. *Adv. Chem. Phys.* **1999**, *106*, 377.